Design, Analysis and Testing of Ionic Wind Propulsion System for an Electric Aircraft

A Major Qualifying Project Report

Submitted to the Faculty of the

WORCESTER POLYTECHNIC INSTITUTE

in Partial Fulfillment of the Requirements for the

Degree of Bachelor of Science

in Aerospace Engineering

by

Cailin Borovicka

Cailin Borovicka

Colleen Henderson

Colleen Henderson

Cole Lederman

Cole Lederman

Ariel Velasquez

Ariel Velasquez

March 21, 2024

Approved by:

Zachary R. Taillefer, Advisor

Assistant Professor of Teaching, Aerospace Engineering Program

WPI

Abstract

This project presents the design of a modular ionic wind propulsion experiment rig with COMSOL simulations and a high-voltage DC-to-DC power converter to provide power to the system. The goal of this project is to explore the parameter space to determine if an optimal electrode configuration(s) exists. This could inform the design of a propulsion system used to propel a lightweight aircraft. The experiment rig must be modular to accommodate many different electrode sizes, shapes, materials, and spacings. The power system must provide enough voltage to generate sufficient thrust for eventual sustained flight. The mechanical design of the experiment apparatus was performed using SolidWorks, while the simulation of ionic wind flow was performed using COMSOL. The modeling of the power converter and battery was performed using LTSpice. Thrust was measured using a digital scale with 0.1 g resolution and wind speed was measured using an anemometer with 0.1 $\frac{m}{s}$ resolution. A benchtop power supply was used for initial testing and the custom power converter was integrated later for comparison. A budget of $1000 was proposed and managed by the team. Ionic wind was generated with a thrust density of up to 321.74 $\frac{mN}{m}$ at 25 kV. Ionic wind was successfully simulated in COMSOL with parameters similar to the experiment rig. It was determined that increasing collector diameter, decreasing the collector-emitter gap without arcing, increasing the quantity of collector-emitter pairs, and staggering the electrodes all increase thrust density for ionic wind.

Acknowledgements

The team would like to thank the following people for their support in accomplishing this project. We would like to thank our advisor, Professor Taillefer, for guiding the team to successfully complete this project. We would also like to thank Dr. Adrianna Hera for training the team in the proper use of COMSOL and Dr. Chu for troubleshooting the COMSOL model.

Table of Authorship

Section	Author(s)	Editor(s)
1. Introduction	Cailin	Colleen
1.1 Defining Ionic Wind Propulsion	Ariel	Cole
1.2 Background & Ionic Wind Propulsion Literature Review	Colleen	Cailin
1.3 Societal Impacts	Cole	Ariel
1.4 Project Goals	Ariel	Cole
1.5 Project Design Requirements and Constraints	Cole, Cailin	Ariel, Colleen
1.5.1 Design Requirements	Cole, Cailin	Ariel, Colleen
1.5.1.1 Power Design Requirements	Cailin	Colleen
1.5.1.2 Propulsion Design Requirements	Cole	Ariel
1.5.2 Design Constraints	Cailin, Cole	Colleen, Ariel
1.5.2.1 Overall Design Constraints	Cole, Cailin	Ariel, Colleen
1.5.2.2 Power Design Constraints	Cailin	Colleen
1.5.2.3 Propulsion Design Constraints	Cole	Ariel
1.6 Project Management	Ariel	Cole
1.7 MQP Objectives, Methods, and Standards	Ariel, Colleen	Cole, Cailin

1.7.1 Propulsion Objectives	Ariel	Cole
1.7.2 Power Objectives	Colleen	Cailin
1.8 MQP Tasks and Timetable	All	All
1.8.1 Gantt Chart	All	All
2. Propulsion Subsystem Analysis and Design	Cole, Ariel	Cailin, Colleen
2.1 COMSOL Model of Ionic Wind	Ariel	Cailin
2.2 Ionic Wind Tunnel Design and Experimentation	Cole	Colleen
3. Power Subsystem Analysis and Design	Colleen, Cailin	Cole, Ariel
3.1 Circuit Design	Colleen	Cole
3.2 Component Selection	Cailin	Ariel
4. Findings, Analysis, and Future Recommendations	All	All
4.1 Wiring and Calibrating the Spellman Power Supply	Cailin	Cole
4.2 Experimental Testing with the Spellman Power Supply	Cailin	Cole
4.3 Construction and Testing of ZVS Driver	Colleen	Ariel
4.4 Construction and Testing of Voltage Multiplier	Colleen	Ariel

4.5 COMSOL Results and Discussion	Ariel	Cole
4.6 Future Recommendations for the COMSOL Model	Ariel	Colleen
4.7 Ionic Wind Experiment Results	Cole	Cailin
5. Conclusions	Cole, Ariel	Cailin, Colleen
6. References	All	All

Table of Contents

Table of Figures

List of Tables

1. Introduction

The majority of current aircraft use a propulsion system that requires some form of hydrocarbon-based fuel. Small aircraft and unmanned aerial vehicles (UAVs) can operate with electric motors but have limited power and range. These propulsion systems typically use an open propellor configuration. These are established and reliable forms of propulsion; however, they have drawbacks. The moving parts in an engine produce a lot of noise pollution and additionally increase the likelihood of mechanical issues arising. Yet the greater repercussion of using hydrocarbon-burning engines is the emissions they produce. In 2022 alone, international aviation emissions exceeded 400 metric tons of CO_2 and continue to increase each year (IEA, 2023). Fortunately, recent research in reducing emissions through the use of electric aircraft has become more prevalent. This project focused on using ionic wind propulsion as primary propulsion for a small aircraft. The investigation of ionic wind propulsion systems in recent years aims to address these drawbacks of traditional aircraft engines. Ionic wind propulsion proposes a new way to produce thrust on an aircraft, with little noise, no moving parts, and no fuel emissions. Several studies and flight tests have been conducted to prove the feasibility of this technology (Vladislav, 2018). While the magnitude of thrust produced by ionic wind propulsion is much smaller than traditional aircraft engines, the outlook is promising for certain unmanned aerial vehicles, such as small aircraft and drones, and for high-altitude applications (Chen, 2019).

The primary goal of this project is to design, build, and test an ionic wind propulsion system that produces measurable thrust. This entails designing and building a modular custom power supply, designing and building a modular experiment model, optimizing an electrode configuration, and simulating ionic wind over the experiment model for varying configurations and parameters.

This project is divided into two sub teams: power and propulsion. Responsibilities of the propulsion sub team include COMSOL simulation, determining power requirements, determining a target thrust value, and designing a modular experiment to measure the produced thrust for different parameters.

Power sub team responsibilities include designing a lightweight, modular, high voltage power system and designing a power supply.

The objectives of this MQP are the following:

1. Design and fabricate a lightweight and modular power system using a DC power supply to provide 20-30 kV.
2. Design and fabricate a modular ionic wind experiment rig to compare the thrust and wind speed output for different electrode configurations and voltage inputs ranging from 0-30 kV.

1.1 Defining Ionic Wind Propulsion

Ionic wind propulsion is a method of creating air flow through a large potential difference between two electrodes. Since it has no moving parts, it is sometimes referred to as a "solid-state" drive. This system is composed of two parallel conductive electrodes. The smaller electrode, referred to as the emitter, serves as a plasma generator and the larger electrode is referred to as the ion collector. The source of plasma occurs from a phenomenon called corona discharge. A corona discharge takes place between an electrode with a sharply curved surface, the plasma emitter, and a larger, less curved surface, the ion collector. The emitter can be charged positively or negatively. The emitter creates a very large electric field which will emit electrons. If the emitter is positively charged, the electrons will return to the emitter while undergoing collisions with air molecules, creating positively charged ions (Wilson, 2009). These ions will be repelled by the emitter and accelerated to the ion collector, Figure 1. In the ion acceleration region, the ions collide with neutral air molecules and transfer momentum (without charge exchange). This momentum exchange results in an aggregate body force in the free stream flow, thus generating an additional acceleration or force on the flow. The resultant force is a thrust on the electrode pair. When the

ions reach the collector electrode, they are neutralized and continue their motion with the air around the electrode (Vladislov, 2018).

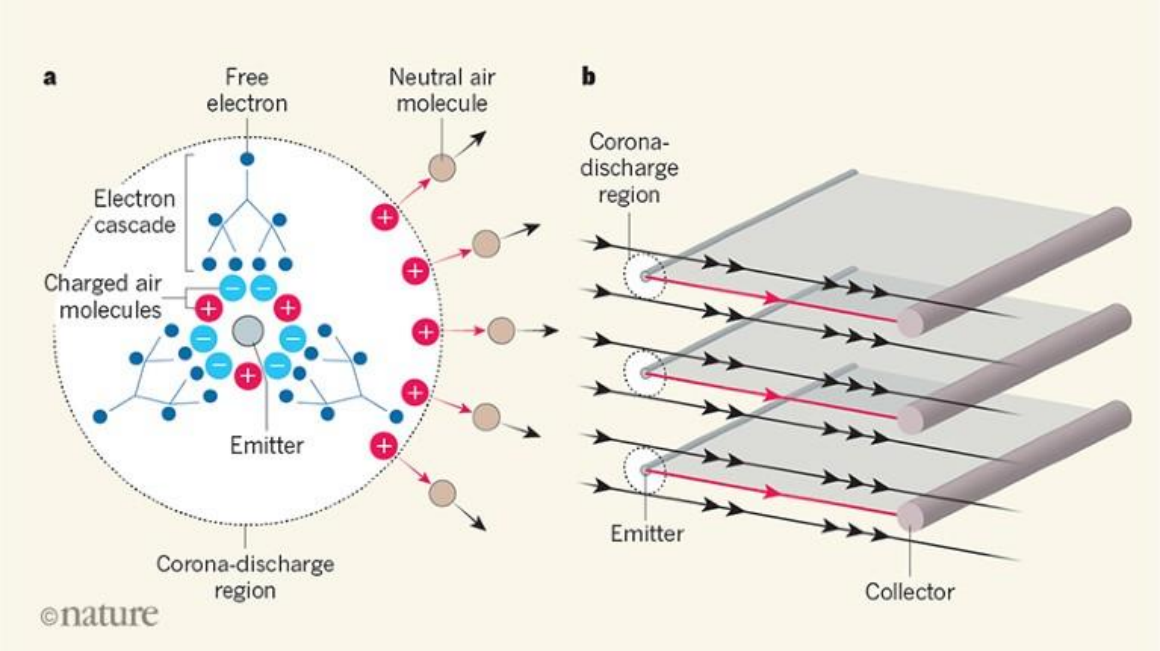

Figure 1: a) Diagram of Corona Discharge around a Wire Electron Emitter. b) Ionic Wind Propulsion (Plouraboue, 2018) ©nature

1.2 Background & Ionic Wind Propulsion Literature Review

In 2018, Massachusetts Institute of Technology, MIT, Professors created a plane powered using ionic wind (Chu 2018). Many experiments before worked towards generating enough thrust to sustain flight, however, this was the first plane to fly without any moving parts. The aircraft weighed approximately five pounds with a five-meter wingspan. The propulsion system consisted of thin positively charged wires strung horizontally facing along the front end of the plane's wing, with thicker negatively charged wires in the back, behind the plane's airfoil wing design. The emitting electrode wires on the front end have a voltage of 40 kilovolts to ionize the air molecules. This voltage is sourced from the onboard power system, which was designed by a team of MIT Professors using batteries as the power source. Their circuit design as well as the plane's design can be seen in Figure 2.

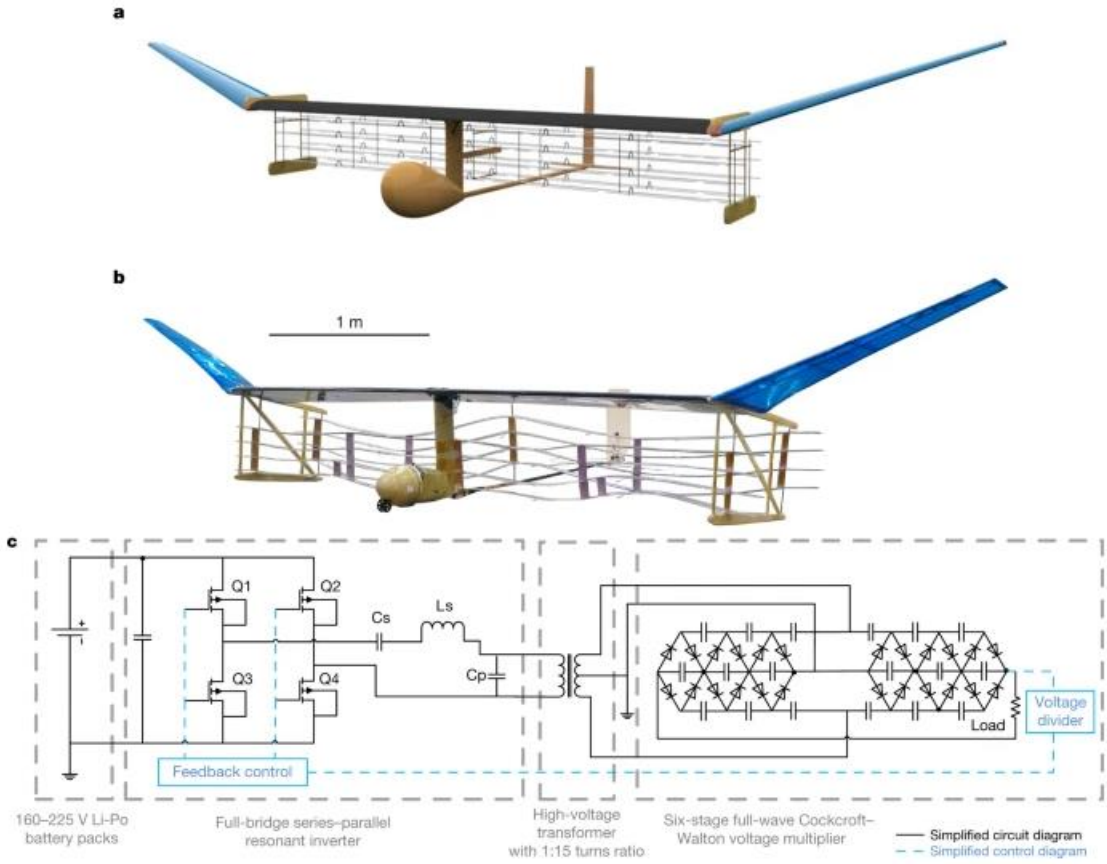

Figure 2: MIT Plane that uses ionic wind propulsion, IWP, computer rendering (a) and actual plane (b), along with the circuit used to supply the voltage to the electrode emitter wires (c) (Xu 2018).

The high-voltage power converter has three stages: a series-parallel resonant inverter to convert 160-225 volts direct current, DC, to high frequency alternating current, AC, a high voltage transformer to step up the AC voltage, and a full-wave Cockcroft-Walton multiplier to convert AC back to DC (Xu 2018).

The plane successfully flew 60 meters across a gym at MIT, repeating ten test flights using a launch device. This plane demonstrated the use of ion propulsion for sustained flight, as well as provided limitations of this model that were used to determine target design requirements such as output voltage and thrust per length. There is future potential to produce more ionic wind using less voltage, increasing the thrust density, and ideally creating an aircraft with no visible propulsion system or control surfaces,

wires, rudders, and elevators, all hidden. Shorter term future goals would be to apply IWP to drones to decrease noise pollution as well as pair IWP with combustion systems for larger aircraft.

Prior research was done by NASA in 2009, where they investigated ionic wind propulsion. A wide array of experiments was conducted, such as varying the electrode emitter, the distance between the emitter and the collector, as well as varying the power supply being DC voltage and not using DC bias (Wilson 2009). Their best experiment utilized a pin array electrode emitter with a 38 mm gap between the emitter and collector, powered by a 22.4 kV output voltage that generated 23 mN of thrust. They concluded that tungsten was preferable to aluminum due to erosion as well as it being one of the five refractory metals, it has a very high resistance to heat and wear and it can produce electrons at very high temperatures. Ultimately, this study concluded that the use of corona discharge was not a practical means of aircraft propulsion. However, many experiments since have sourced this NASA study have produced higher thrust ratios.

Further feasibility studies were done by hobbyists. Several YouTube videos were consulted, showing experiments, and visually demonstrating the concept of ionic wind propulsion. An experiment that produced a very notable amount of thrust was from Jay Bowles from the Plasma Channel on YouTube. Bowles works with many kinds of experiments on his channel and produced two ionic plasma thrusters. In his most recent experiment, he measured the exiting wind velocity to be 4 [m/s] using a circuit he made (Bowles 2023). The circuit consisted of a 15 V power source connected to a flyback transformer connected to a voltage multiplier of about 8 kV to produce an output voltage of 50 kV. This is especially useful to consult, it's a very simple yet effective circuit design. His propulsion system made use of a nozzle arrangement with thin wires for the electrode emitters and thicker tubes for the cathode collectors. He used a non-linear, staggered arrangement between the electrode emitter and collectors with a 25 mm spacing between them. With a final measurement of 0.216 N of thrust generated, it's a great success towards ionic wind propulsion being able to generate enough thrust to fly a small plane.

A common variable to compare across experiments was the thrust per length [mN/m]. In the experiments researched, the ratio ranged from 60 to 870 [mN/m]. The 870 [mN/m] thrust per length was

an electrode configuration experiment done in December of 2022 from Graz University of Technology. They investigated an electroaerodynamic (EAD) airplane with a biplane wing design. They tested two electrode configurations, a single electron emitter and a grounded cathode collector, and two electron emitters and three cathode collectors. With an output voltage of 55 kV, they were able to generate about 8.5 N of thrust at a distance of 60 mm (Estahbanati 2022). The higher the thrust per length the more efficient the propulsion system is, which is an important parameter in narrowing down the consulted experiments towards a propulsion design focus.

1.3 Societal Impacts

Elimination of hydrocarbon-based propulsion systems from aircraft has many possible societal impacts including improvements in aircraft simplicity, fossil fuel use reduction, climate change mitigation, and noise pollution mitigation. Ionic wind propulsion does not have such broad capability or applicability that it could replace propulsion systems used in high thrust applications; however, it has many advantages for small aircraft with low thrust requirements. First, the fact that there are no moving parts in an ionic wind propulsion system increases simplicity for aircraft design and reduces the likelihood of mechanical failure. A decrease in the frequency of mechanical failures would result in less catastrophic incidents and overall safer air travel.

In addition to improving aircraft simplicity, ionic wind propulsion also has the potential to contribute to the broader goal of the aerospace industry to reduce carbon emission. While it has not been demonstrated that ionic wind propulsion could completely replace conventional propulsion systems, it could provide an alternative for lower thrust applications. Conventional jet engines require large amounts of fuel. Jet fuels typically consist of various crude oil petroleum distillation products like naphtha, gasoline, or kerosene (Agency for Toxic Substances and Disease Registry, 1995, p. 75). As a result, the aerospace industry is a large user of fossil fuels and natural oil. Furthermore, aviation accounted for 2% of global energy-related CO_2 emissions in 2022, exhibiting faster carbon emission growth than rail, road, or shipping (International Energy Agency, 2023). In that year, aviation emissions reached nearly 800

Million Tonnes of CO_2 (International Energy Agency, 2023), making the aviation industry one of the fastest-growing sources of greenhouse gas emissions and driving global climate change (World Wildlife Fund, n.d.). Ionic wind propulsion requires no fuel. This means that widespread adoption of ionic wind propulsion could slightly reduce carbon emissions by the aircraft industry.

Lastly, ionic wind propulsion limits aircraft noise pollution. Moving propellers and jet engines are noisy and irksome for surrounding residents and wildlife. A recent study conducted at the University of California San Diego found that high-frequency noise created by drones could cause temporary hearing loss in certain species of whales, possibly impacting their ability to communicate or hunt. The study also noted that drone presence caused some bird species to fly away from their nests and foraging areas, potentially disrupting their nesting cycles or breeding (Frackiewicz, 2023). Moreover, NASA conducted a psychoacoustic test to explore differences in subjective response to noise from flyovers of small unmanned aerial systems (sUAS) with noise from drive-bys of road vehicles encountered in residential neighborhoods, after which researchers concluded that there may be a systematic difference between the annoyance response generated by the noise of sUAS and road vehicles. This experiment indicated that noise from sUAS may cause more annoyance to residents than road vehicles (Christian et al., 2017). Available research findings consistently suggest that drone noise is more annoying than road or aircraft noise, due to the tonal characteristics and the presence of high-frequency broadband noise (Civil Aviation Authority, 2023, p. 28). There is even sufficient scientific evidence that noise exposure can induce hearing impairment, hypertension and ischemic heart disease, annoyance, sleep disturbance, and decreased school performance (Passchier-Vermeer et al., 2000). Since an ionic wind propulsion system uses no moving parts there is little noise associated with this system. Although the thrust produced by ionic wind propulsion is currently too small to use on large aircraft, the thrust is sufficient to power drones and small aircraft. Modern drone technology radiates an unpleasant humming noise and the increasing use of drones in cities might disturb urban residents or wildlife both mentally and physically.

An ionic wind propulsion drone would be practically silent and much more considerate of nearby residents.

After analyzing existing studies regarding the impacts of aircraft and drones on fossil fuel consumption, carbon emissions, and noise pollution it is evident that further development of ionic wind propulsion technology would substantially benefit the wellbeing of humans, wildlife, and the environment.

1.4 Project Goals

- Design, build, and test an electric propulsion system for unmanned aerial vehicle (UAV) or drone.
- Work as a team to design, build and test a moderately complex aerospace system in which the overall vehicle performance is critically tied to the mass and performance of the individual components and assemblies.
- Apply software tools: COMSOL, SolidWorks, PSpice, LTSpice, LabVIEW, and others.
- Apply manufacturing techniques: 3D printing, laser cutting, drill pressing, soldering

1.5 Project Design Requirements and Constraints

1.5.1 Design Requirements

1.5.1.1 Power Design Requirements

- The power subsystem outputs a voltage in the range of 20-30 kV. A lower voltage will not produce the required thrust, and a higher voltage may be unnecessary or possibly cause arcing.
- A bench top power supply is operated in parallel with a custom circuit design to ensure testing of the propulsion system can be conducted in a timely manner.
- This output voltage is adjustable.
- The power output values measured for the power subsystem are consistently repeatable.

1.5.1.2 Propulsion Design Requirements

- The experiment rig is modular so that different electrode sizes, shapes, spacings, materials, and configurations may be tested.
- The experiment rig produces ionic wind with a thrust density of at least 60 $\frac{mN}{m}$ using 20-30 kV of voltage.
- Thrust is measured with a resolution of 0.1 g.
- The thrust values measured are consistently repeatable.
- The COMSOL simulation of ionic wind converges and generates thrust values for comparison to experimental results.

1.5.2 Design Constraints

1.5.2.1 Overall Design Constraints

- The overall ionic wind propulsion system adheres to an allotted budget of $1000.
- The overall ionic wind propulsion system is modular for ease of manufacturing, assembly, maintenance, and adjustment.

1.5.2.2 Power Design Constraints

- The power subsystem is modular for ease of manufacturing, construction, maintenance, and adjustment.

1.5.2.3 Propulsion Design Constraints

- The propulsion subsystem adheres to an allotted budget of $500.
- The propulsion subsystem is modular for ease of manufacturing, assembly, maintenance, and adjustment.

1.6 Project Management

For this project, the following sub teams were held:

1. Power Sub Team

    a. Circuit Component Selection (Cailin Borovicka)

    b. Circuit Modeling (Colleen Henderson)

2. Propulsion Sub Team

    a. 3D Computer-Aided Design, Manufacturing, and Assembly (Cole Lederman)

    b. COMSOL Ionic Wind Simulation (Ariel Velasquez)

Weekly meetings were held in person to facilitate communication between the sub teams. Furthermore, Cole Lederman was the Lab Lead and Cailin Borovicka was the Lab Safety Lead.

1.7 MQP Objectives, Methods, and Standards

1.7.1 Propulsion

1. Design and fabricate a modular and easily replicable ionic wind experiment rig to produce 60 $\frac{mN}{m}$ of thrust using 20-30 kV of voltage and compare the thrust for different electrode configurations.
    a. Generate a CAD model using SOLIDWORKS and use inexpensive, readily available materials to create and build a test setup for determining the optimal electrode configuration, geometry, spacing, and material.
    b. Design an experimental procedure and test matrix.
2. Simulate the ion flow over the electrodes using COMSOL.

1.7.2 Power

1. Design and fabricate a lightweight and modular power system using a DC power supply to provide 20-30kV of voltage.

a. Research current and voltage range of power supplies from past experiments.

b. Determine optimal modular circuit components.

c. Simulate circuit on modeling software to meet design requirements.

    i. Experiment software includes: LTSpice, Cadence Allegro, and Multisim.

d. Finalize circuit design and components through test simulations.

e. Operate benchtop power supply in parallel with custom circuit.

1.8 MQP Tasks and Timetable

1.8.1 Gantt Chart

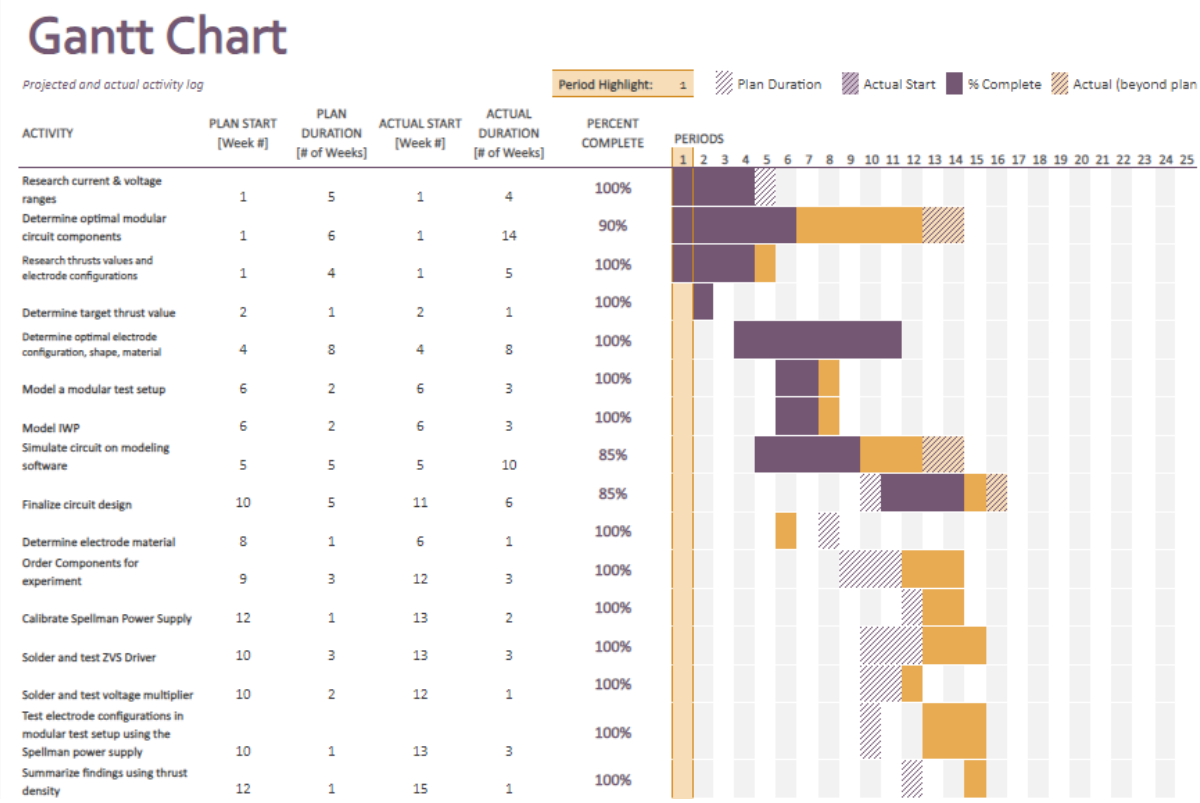

Figure 3: Project Gantt Chart

2. Propulsion Subsystem Analysis and Design

2.1 COMSOL Model of Ionic Wind

2.1.1 Mathematical model

The purpose of the COMSOL model is to create a simulation to study the physical changes in a two-dimensional field of the electrode system of the aircraft. Multiple ionic wind simulations have been created to model propulsion systems like this and ionic wind cooling machines. In this work, the electrode model will be used on the aircraft, which includes a wire and airfoil structure. The goal of the model is to compute ionic wind, space charge density, and potential distribution. The model will be used to discover the dependence of ionic wind on the applied voltage, wire/electrode radius, and electrode gap and height. The simulation geometry and results are based on the proposed physical model and its corresponding experimental setup. Consistency with the research results in the references mentioned was also considered.

As shown in section 2.2 Ionic Wind Tunnel Design and Experimentation**,** the experimental model is a rectangular domain composed of a stainless steel 316 wire emitter electrode and hollow aluminum cylinders of varying radii for the collector electrode. A high DC voltage is applied to the wire electrode, and an opposite DC voltage is applied to the collector electrode. When corona discharge occurs at the wire electrode, an airflow with a certain velocity will be felt behind the collector electrodes. When the applied voltage is high enough, the electrode system will create thrust, and the thrust can be measured.

To easily solve the ionic wind propulsion system model, multiple assumptions must be made (Zhang, 2022).

1) The gas medium is simplified to only consider the movement and distribution of anions.
2) The ion mobility is constant and not affected by the electric field.
3) The thermal diffusion of ions is ignored.
4) Laminar flow, room temperature, low speed, and low Reynolds number are assumed.

5) The simulation model is a steady-state process.

The modeling of ionic wind includes electrostatics, fluid dynamics, and charge transfer motion to create an electrohydrodynamic flow. The following governing equations can be derived and are only applicable to the drift region (2.1) to (2.4) (Huang, 2018). The drift region is the area between the wire electrode and collector electrode where the ions collide with the neutral air molecules.

Applying a voltage to the surface of the emitter wire will generate an electric field in the area near the electrode. The distribution of potential difference V between the two electrodes are controlled under the space charge through the following Poisson equation:

$$\nabla^2 V = -\frac{\rho_q}{\varepsilon_0} \tag{2.1}$$

Where V is the potential difference, ρ_q (C/m^3) is the space charge density and ε_0 is the vacuum dielectric constant.

The electric field E is calculated as:

$$E = -\nabla V \tag{2.2}$$

The current density J is calculated from the space charge density in the drift region as:

$$J = \mu E \rho_q + \rho_q u - D_i \nabla \rho_q \tag{2.3}$$

Where μ is the mobility of ions under the electric field, u is the air velocity vector, and D_i (m^2/s) is the ion diffusion coefficient. However, since the electric field is relatively low, and conduction is more influential than convection and ion diffusion, (3) can be simplified to:

$$J = \mu E \rho_q \tag{2.4}$$

Also, the current density should satisfy the charge continuity equation:

$$\frac{\partial \rho_q}{\partial t} + \nabla \cdot J = 0 \tag{2.5}$$

Since the simulation is based on the DC corona discharge, (5) can be simplified under the steady-state conditions as:

$$\nabla \cdot J = 0 \tag{2.6}$$

Considering equations (1), (2), (5), and (6), the relationship for the space charge density in the drift region can be written as:

$$\nabla \rho_q \cdot \nabla V - \frac{{\rho_q}^2}{\varepsilon_0} = 0 \tag{2.7}$$

Previous experiments have generally demonstrated an ionic wind of less than 10 m/s. Therefore, it is assumed that the fluid is incompressible laminar in the drift region. It is also assumed that the incompressible flow decouples the energy conservation from the momentum equation. Considering a fixed air viscosity, the Navier-Stokes equation can be written as:

$$\rho \frac{\partial u}{\partial t} + \rho(u \cdot \nabla)u = -\nabla p + \nabla(\nabla u + (\nabla u)^T) + F \tag{2.8}$$

Where ρ is the air density, p is the pressure, and F is the volumetric force created by the charged particles generated by the electric field force colliding with neutral air particles creating a momentum transfer. Under fluid stability conditions, the transient term on the left side of (8) is 0, and (8) is simplified to:

$$\rho(u \cdot \nabla)u = -\nabla p + \nabla(\nabla u + (\nabla u)^T) + F \tag{2.9}$$

Under the direct current condition, magnetic field strength can be ignored, and the total force per unit air volume can be expressed as (Zhang, 2022):

$$F = \rho_q E = -\rho_q \nabla V \tag{2.10}$$

Then, (10) can be described as:

$$\rho(u \cdot \nabla)u = -\nabla p + \mu \nabla^2 u + \rho_q E \tag{2.11}$$

Where considering a fixed air density, the fluid mass continuity equation for an incompressible fluid can be simplified to:

$$\nabla \cdot u = 0 \tag{2.12}$$

By substituting (3) into (6), the charge transport equation can be obtained as:

$$\nabla \cdot \left(\rho_q \mu E + \rho_q u - D_i \nabla \rho_q\right) + u \nabla \rho_q = \nabla \cdot J = 0 \tag{2.13}$$

The boundary conditions have been adjusted for the mathematical model above. Furthermore, the thickness of the ionization region is ignored.

The electric field intensity of corona discharge on the wire electrode is determined using Peek's law. For a positive corona discharge, Peek's empirical formula can be used to calculate the electric field strength E_p (V/m) on the surface of an ideal, smooth cylindrical electrode with radius r_c as:

$$E_p = E_0 \delta \varepsilon \left(1 + \frac{0.308}{\sqrt{\delta r_c}}\right) \tag{2.14}$$

Where E_0 = 3.31 $\times 10^6$ V is the air breakdown electric strength, δ = 298 p/T is the relative air density, T = 293.15 K, and p = 1 atm. ε is the electrode's dimensionless surface roughness, but it is assumed to be ideal smooth there the value is equal to 1.

The surface charge density is calculated by specifying the applied voltage V and assuming the electric field E_p on the wire electrode's surface. When the space charge density is low, the electric field $E(r)$ in the ionization region can be given by:

$$E(r) = \frac{E_p r_c}{r} \tag{2.15}$$

Where r is the radial position starting from the center of the wire electrode.

According to Kaptsov's hypotheses, E_0 is the electric field intensity at the ionization region boundary and the drift region (Huang, et al., 2018). The ionization region radius r_i is obtained from manipulating equations (17) and (18) as:

$$r_i = \frac{E_p r_c}{E_0} = r_c \delta \varepsilon \left(1 + \frac{0.308}{\sqrt{\delta r_c}}\right) \tag{2.16}$$

Further, by integrating the electric field between r_c and r_i , the voltage V_i applied to the wire electrode surface is obtained by:

$$V_i = V_c - E_p r_c \ln\left(\frac{E_p}{E_0}\right) \tag{2.17}$$

Where E_0 is the voltage planned to be applied to the wire electrode.

The mathematical model is presented using COMSOL Multiphysics 6.1 multiphysical field coupling software to perform the finite-element simulation calculations. The ionic wind model includes the electrostatic mode to solve the Poisson equation and calculate the potential distribution between the electrodes. The charge transport mode is used to solve the charge transport equation and calculate the space charge density distribution. Finally, the laminar flow mode is used to solve the Navier-Stokes equation of the incompressible fluid and obtain the ionic wind's velocity.

2.1.2 Geometrical Model

Figure 4 shows the simulation model in the 2-D Cartesian coordinate system. To simplify the model, it is assumed that the side view of the emitter wire and collector electrode have an infinite length, parallel cylinder. The simulation domain is a rectangle with a width of 200 mm and a height of 70 mm with its center at (80,0) mm. The wire electrode is zeroed on the x-axis while the y-axis varies depending on the experiment. The radius r_c is 0.2032 mm. The collector electrode's size and location depend on the experiment. The geometric model uses a finer mesh to accurately simulate the minute changes around the electrodes. The regions further away from the electrodes have meshes sparsely divided to help with a fast calculation speed. The mesh in Figure 4 has 5439 domain elements.

A) For Boundary 1 (wire electrode), a constant voltage V_c is set to +30 kV.

B) Boundaries 2 and 3 are the upper and lower walls. The electric potential, space charge density, and surface airflow velocity is set to 0.

C) Boundaries 4 and 6 are set with the open boundary condition. The potential and ion transport conditions are the same as boundaries 2 and 3.

D) Boundary 5 is set as a grounded wall and an ionic diffusion flux of 0.

E) Finally, all boundaries have a no slip condition. The pressure and temperature for the domain are 1 atm and 293.15 K, respectively.

When inputting equation (10) into COMSOL, create a volume force under the Laminar Flow module, and input the function *ct.Fehdx* into the x-axis field and *ct.Fehdy* into the y-axis field. Also, right click the Multiphysics module and add the electrode physics. Change the necessary parameters to the values shown in Table 1 and select the components of Boundary 1.

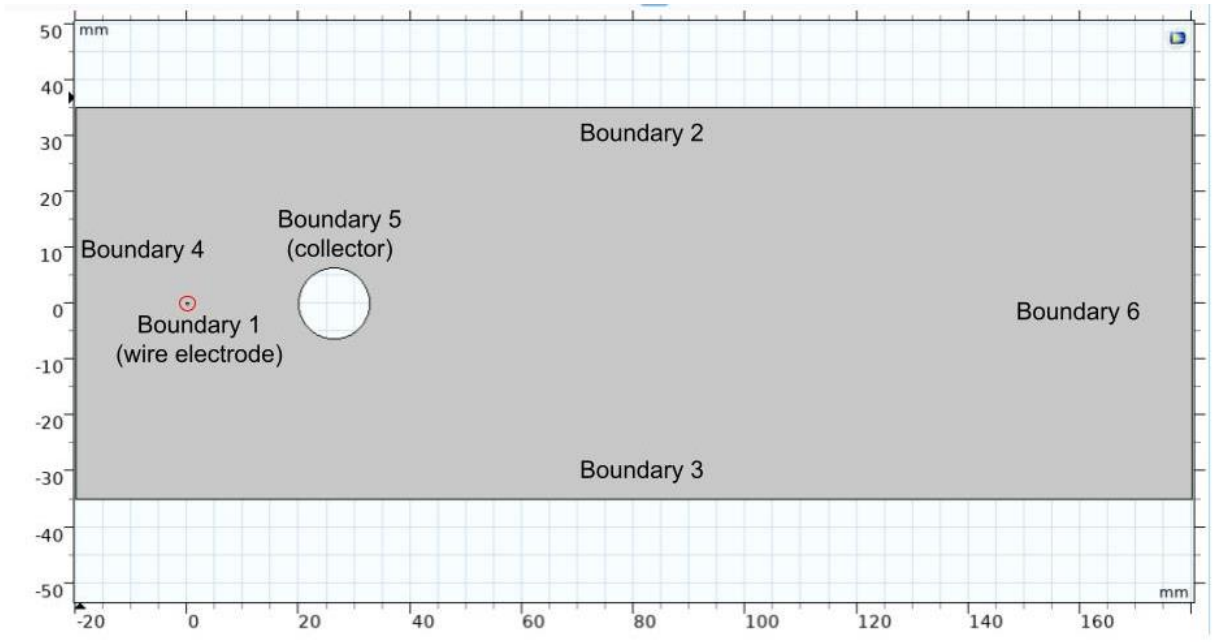

Figure 4: Geometric model of Ionic Wind Simulation

Table 1 shows the relevant simulation parameters. Adjusting the simulation boundary conditions is necessary to obtain the ionic wind's Multiphysics characteristics.

Table 1: All the Parameters for Simulation

Parameters	Value
Air density (1 atm, 293.15 K), ρ	1.205 kg/m^3
Dynamic viscosity (1 atm, 293.15 K), μ	1.8×10^{-5} Ns/m^3
Relative permittivity, ε_r	1
Reduction ion mobility coefficient, μ_{i0}	3×10^{21}/V·m·s
Ion diffusion coefficient, D	5.19×10^{-5} m^2/s
Initial value for space charge density, ρ_q	10^{-5} C/m^3
Wire electrode radius, r_c	0.2032 mm
Collector electrode radius, r_w	0.25 in
Wire electrode voltage, V_c	+30 kV

2.1.3 Solving the Geometrical Model

When trying to solve the simulation model, there were recurring problems where the model would not converge. To solve this issue, the team implemented a segregated approach to solve the model in steps and use the previously solved solution as an initial guess to get as close as possible to the answer and allow COMSOL to converge on a solution.

1) Create a second volume force under the Laminar Flow module with a value of 1, and the volume force from *ct.Fehd* is disabled. Study 1 will only solve the Laminar Flow module with the arbitrary volume force as an initial guess. Compute Study 1.

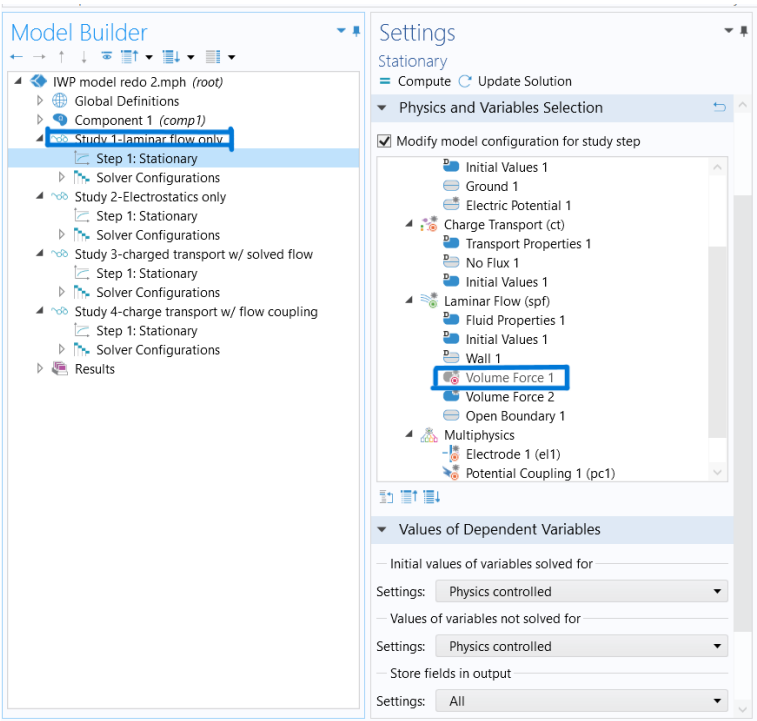

Figure 5: Step 1 of the Segregated Solver Method

2) Apply an electric potential of 30 kV to the wire emitter. Study 2 will only solve the Electrostatics module and the electric potential of the wire emitter. Under "Values of Dependent Variables," set the "Values of variables not solved for" to "User controlled" and set the study to Study 1. Compute Study 2.

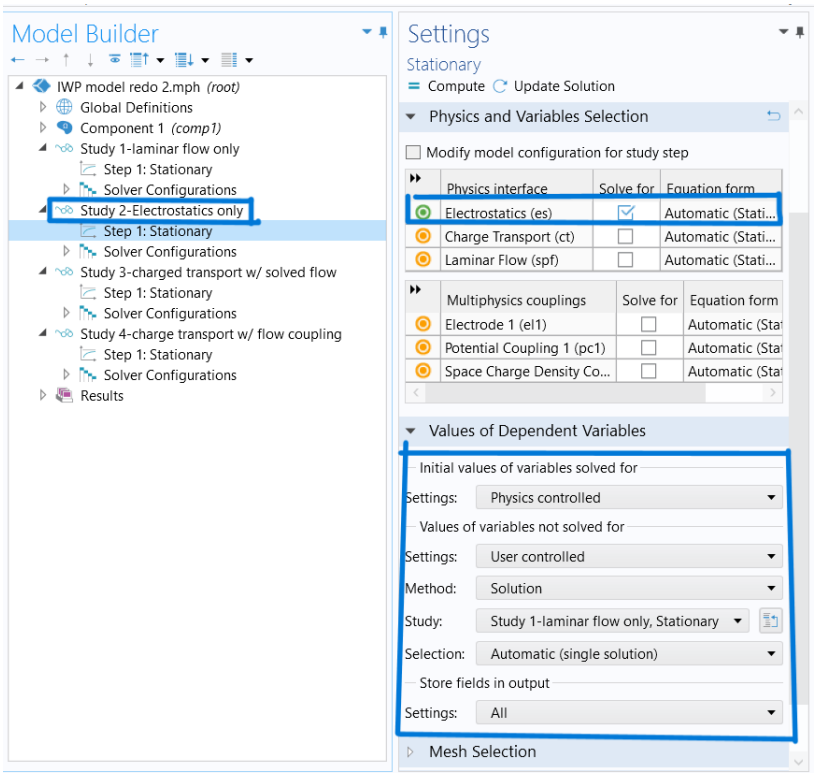

Figure 6: Step 2 of the Segregated Solver Method

3) Disable the electric potential parameter given to the wire emitter and disable the Laminar Flow module in the solver. Study 3 will solve for the Charge Transport physics using the solved Laminar Flow and Electrostatics physics. Under “Values of Dependent Variables,” set both the “Initial values of variables solved for” and “Values of variables not solved for” to “User controlled” and set the study to Study 2. Compute Study 3.

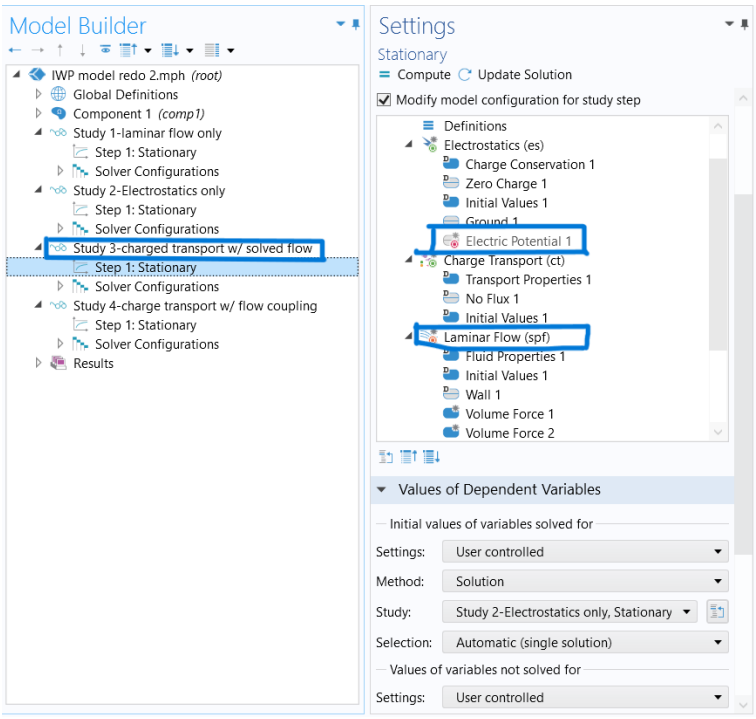

Figure 7: Step 3 of the Segregated Solver Method

4) Disable the electric potential parameter given to the wire emitter and disable the volume force parameter set as 1. Enable the volume force parameter set as *ct.Fehdx*. Study 4 will solve all the physics together using the initial values from the solutions previously solved for. Under "Values of Dependent Variables," set the "Initial values of variables solved for" to "User controlled" and set the study to "Study 3." Compute Study 4.

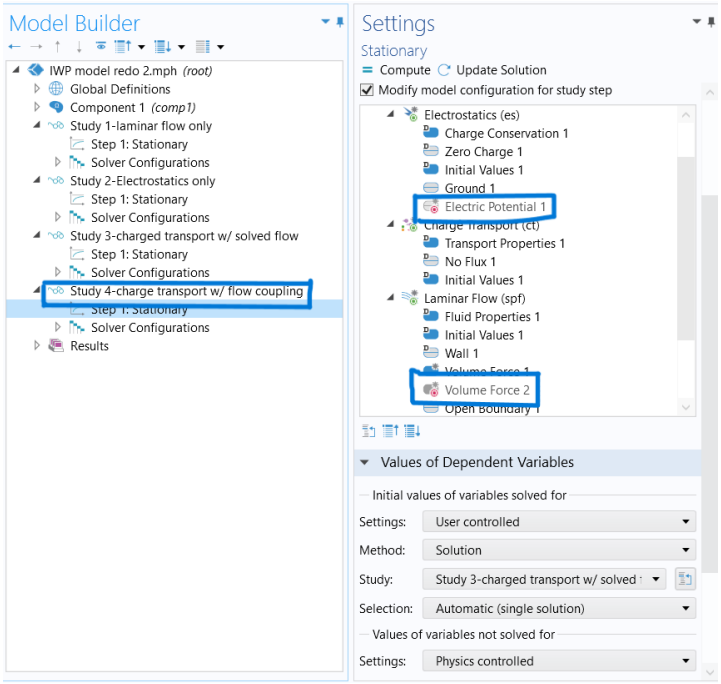

Figure 8: Step 4 of the Segregated Solver Method

5) A good practice was to change the parameters of the domain in small increments, like changing the electrode gap in a small increment, then building the geometry and immediately computing Study 4. The model will use the previous domain geometry as an initial guess, which will help the model converge much quicker. If this does not work, then solve the model again starting with step 1.

When solving the simulation, the electrode gap, electrode voltage, and radius of the collector electrode were varied in small increments to plot the change in velocity and volume force. These parameters propel the plane forward and optimizing them will create the most propulsion for the plane. The independent parameters were changed in small increments to ensure the model was able to converge. Large changes would create an error message since the model would fail to converge.

2.2 Ionic Wind Tunnel Design and Experimentation

2.2.1 Experiment Goals

To optimize the propulsion system, an experiment was designed to test different electrode configurations, spacing, materials, and geometry. The end goal of this experiment is to produce plots of thrust vs voltage for different electrode configurations. Therefore, the experimental apparatus should account for the measurement of thrust. It was decided that this experiment should be modular so that many different electrode design variables could be tested now and in the future by other researchers.

2.2.2 Experiment Design

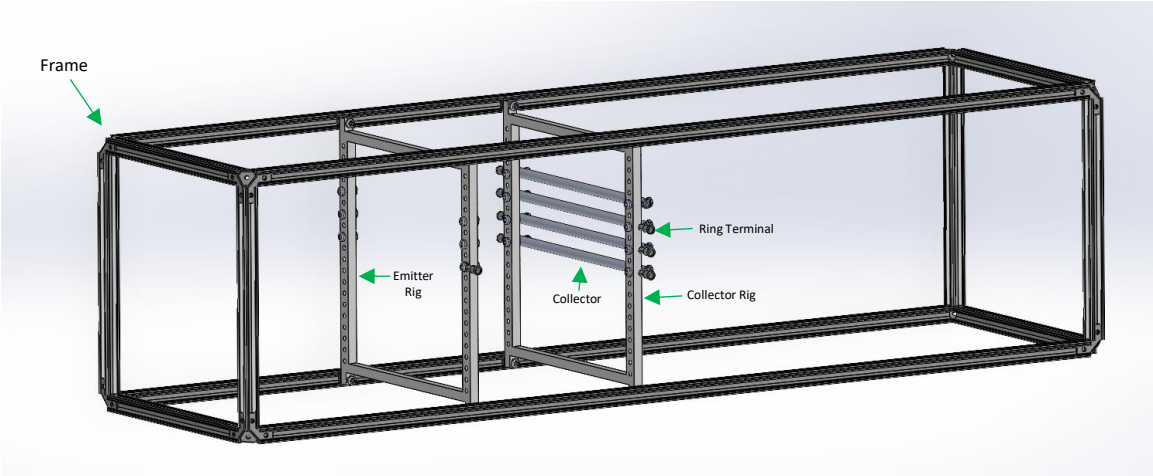

Figure 9: Ionic Wind Experiment CAD Model

The final rig design (Figure 9) is essentially an “ionic wind tunnel”. It consists of a frame assembly, an emitter rig, a collector rig, and an acrylic enclosure. For thrust measurement, the entire ionic wind tunnel can be turned upright and placed on a digital scale so that the ionic wind is flowing upward and the rig is propelled downward toward the scale.

The frame assembly is composed from miniature t-slotted anodized aluminum framing with a 10 mm rail height. Anodized aluminum was selected to prevent arcing to the frame. Its dimensions are 6 inches by 6 inches by 24 inches. The framing rails are connected via eight 3-way corner brackets.

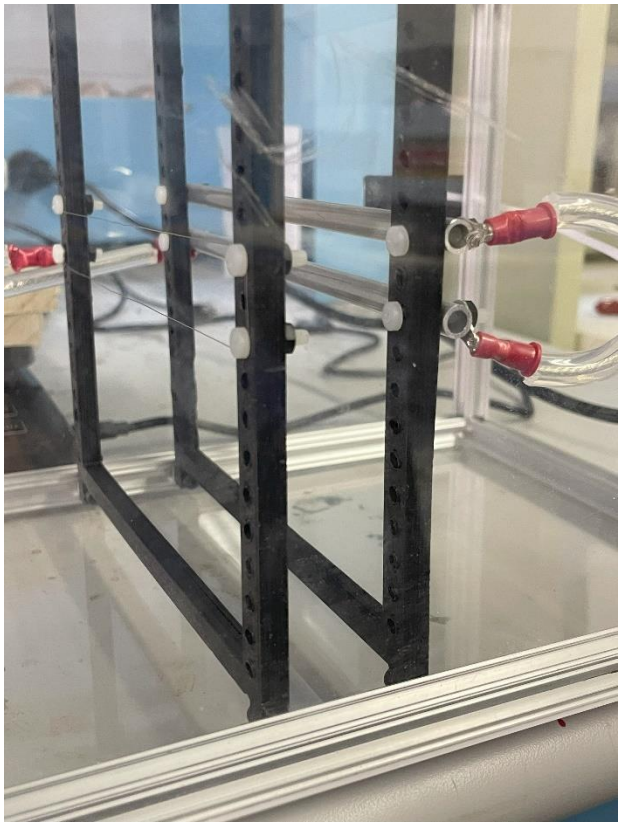

Figure 10: Close-up of Emitter and Collector Rigs

The emitter rig is 3D printed out of polylactic acid, or PLA, a common printing filament. It has a series of holes for mounting the emitter wire as shown in Figure 10. Power is provided to the emitter rig through 18-gauge insulated high voltage wire and a single ring terminal, which is mounted on one of the holes. The emitter wire is wrapped around a series of screws corresponding to the desired emitter configuration. 32 AWG bare stainless steel 316 wire is used for the emitters in this experiment, but this can be varied for future experimentation. Sliding nut plates and screws are used to fasten the emitter rig to the frame and allow for changes in spacing between the emitter and collector.

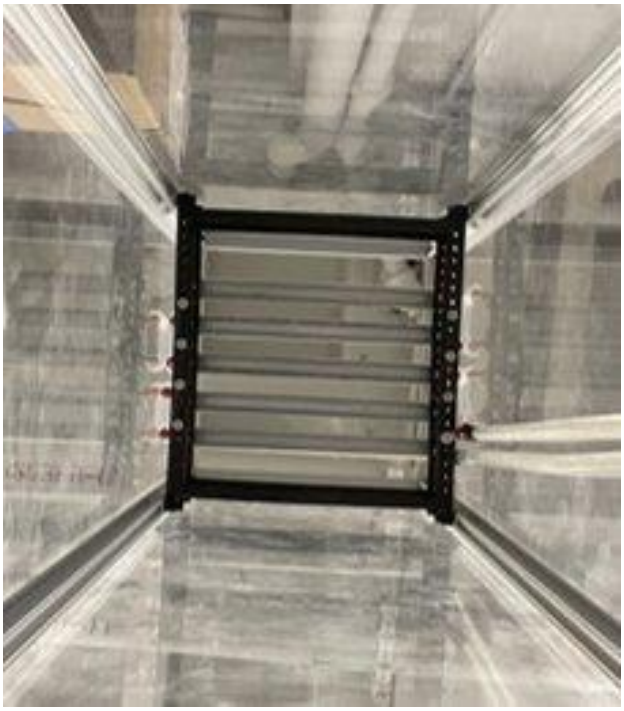

Figure 11: View of Experiment Rig from Scale

Figure 12: Drill Pressing Mounting Holes in Collectors

The collector rig is also 3D printed out of PLA. Like the emitter rig, it has a series of holes for mounting the collectors (Figure 10). Power is provided to the collectors through 18-gauge insulated high voltage wire and a single ring terminal. Aluminum tubing was used for the collectors in this case, but this can be varied for future experimentation (Figure 11). Holes are drill pressed on each end of the tubing for mounting (Figure 12). The holes were drilled all the way through for the $\frac{1}{4}$ inch collectors, but only one side of the collector was drilled for the other two sizes. This was because the hex nuts could fit inside the larger collectors and thread onto the screw, while the nuts could not fit inside the $\frac{1}{4}$ inch collectors. The collectors are mounted to the collector rig by nylon screws to avoid producing unwanted corona discharges. The collectors are electrically connected to each other through ring terminals placed on the mounting screws and 18 gauge insulated high voltage wire. Sliding nut plates and screws are used to fasten the collector rig to the frame and allow for changes in spacing between the emitter and collector.

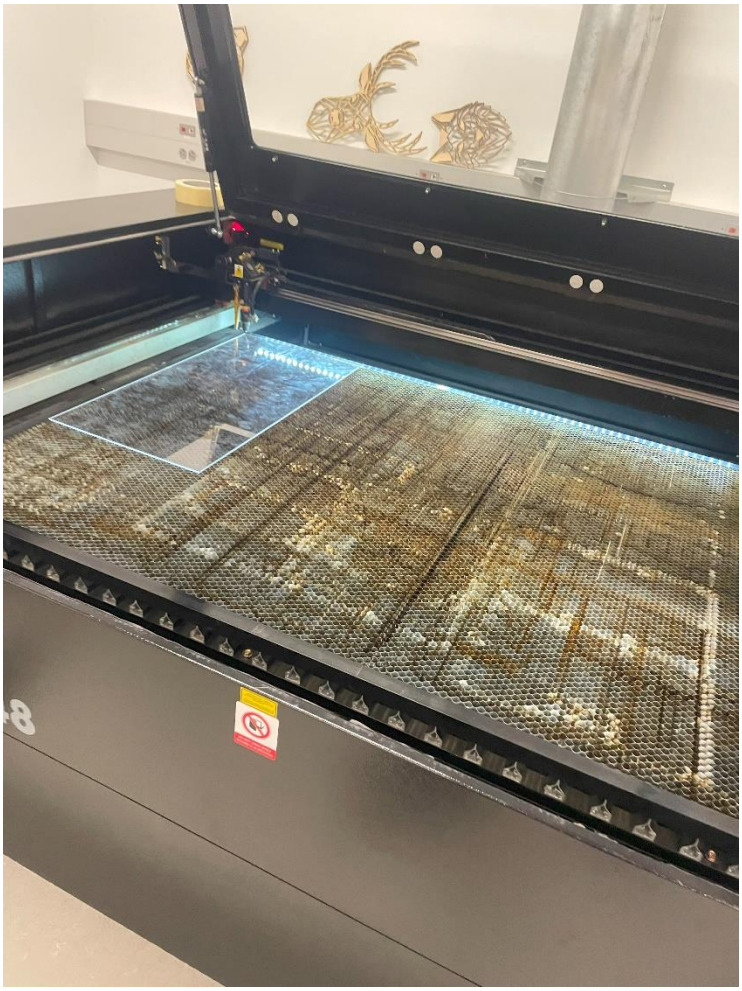

Figure 13: Laser Cutting Acrylic Enclosure

To optimize airflow and prevent injury from arcs or contact with charged metal, there is an enclosure around the ionic wind tunnel. This enclosure is made from $\frac{1}{8}$ inch laser cut acrylic sheets with fabricated mounting holes (Figure 13). The enclosure is mounted to the frame assembly through the same nut plates and screws used to fasten the collector and emitter rigs to the frame.

2.2.3 Experimental Procedure

Table 2: Experimental Tests and Parameters

Test #	Voltage Range (kV)	Collector Diameter (in)	# of Collectors	# of emitters	Linear or Staggered	Collector Spacing (mm)	Collector-Emitter Gap (in)
Collector Diameter							
1	0-25	$\frac{1}{4}$	1	1	Linear	N/A	1.5
2	0-25	$\frac{3}{8}$	1	1	Linear	N/A	1.5
3	0-25	$\frac{1}{2}$	1	1	Linear	N/A	1.5
Collector-Emitter Gap							
4	0-25	$\frac{1}{2}$	1	1	Linear	N/A	0.875
5	0-25	$\frac{1}{2}$	1	1	Linear	N/A	3
Electrode Quantity							
7	0-25	$\frac{1}{4}$	2	2	Linear	10	1.5
Electrode Staggering							
12	0-25	$\frac{1}{4}$	1	2	Staggered	N/A	1.5
14	0-25	$\frac{1}{4}$	2	1	Staggered	10	1.5
Collector Spacing							
16	0-25	$\frac{1}{4}$	2	1	Staggered	30	1.5
17	0-25	$\frac{1}{4}$	2	1	Staggered	50	1.5
18	0-25	$\frac{1}{4}$	2	1	Staggered	70	1.5

There are many design parameters that can be adjusted to produce different levels of ionic wind. This experiment was limited by budget constraints and fabrication methods. Therefore, only a handful of possible parameters were tested (Table 2). There are gaps in the numbering scheme for the tests because

some tests were removed in the interest of time. The ranges for the parameters such as the electrode configuration, voltage, collector diameter, electrode gap, and electrode spacing were selected based on a literature review of previous ionic wind electrode configuration experimentation to replicate results and verify trends. In theory, a higher voltage, larger collector diameter, smaller electrode gap, and smaller electrode spacing should all contribute to an increase in thrust. All parameters were tested at power levels from 0-25 kV.

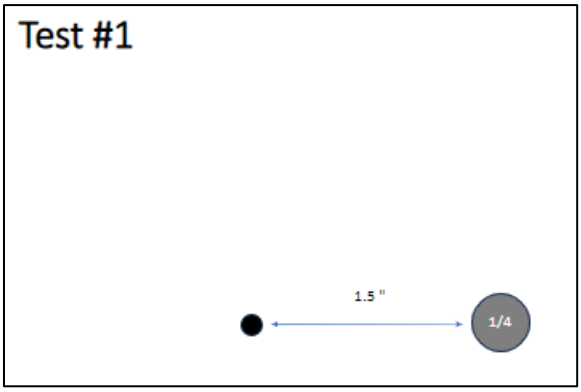

Figure 14: Test Configuration #1

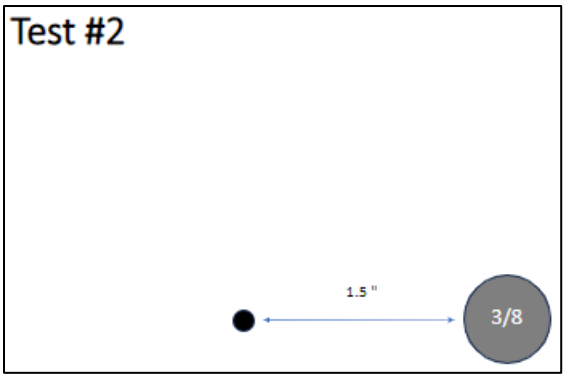

Figure 15: Test Configuration #2

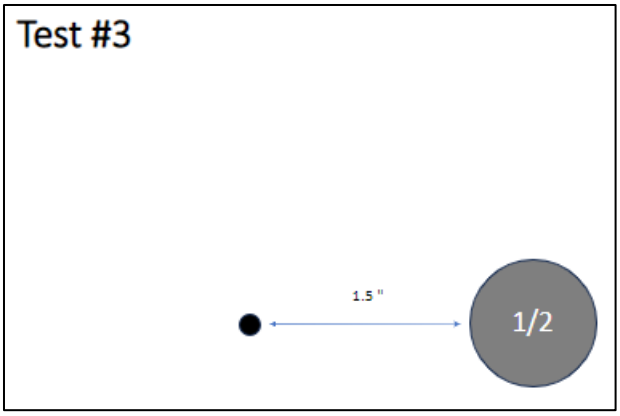

Figure 16: Test Configuration #3

The first parameter tested was the electrode geometry. For this experiment, a constant emitter geometry of 32 AWG wire was used. However, the diameter of the collector tubes was varied. Collector diameters of ¼ inch (6.35 mm) (Figure 14), 3/8 inch (9.525 mm) (Figure 15), and ½ inch (12.7 mm) (Figure 16) were tested. These diameters were selected to try to prove that increasing the ratio of the diameter of the collector divided by the diameter of the emitter increases thrust. Prior experiments have used collector diameters from ¼ inch to ¾ inch. The diameters for this experiment were selected accordingly to try to replicate these relationships. Other geometries, including aluminum airfoils, were considered for the collectors. However, manufacturing constraints caused the team to pivot away from this option. Other geometries can be tested in future experiments as long as they have mounting holes that align with the collector rig.

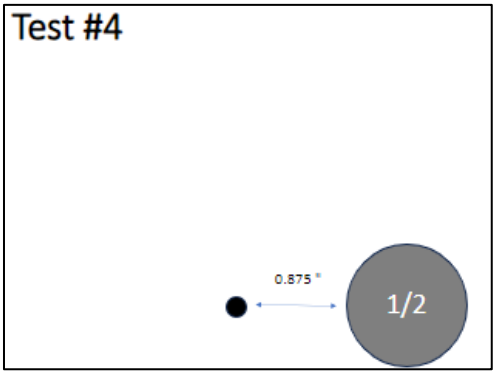

Figure 17: Test Configuration #4

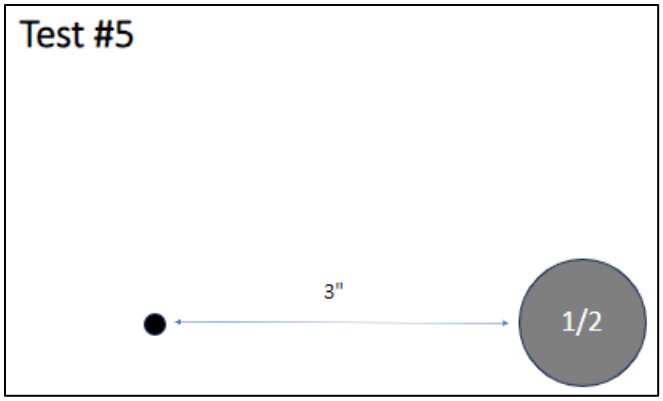

Figure 18: Test Configuration #5

The second variable is the collector-emitter gap. For this experiment, collector-emitter gaps of 0.875 inches (Figure 17), 1.5 inches (Figure 16), and 3 inches (Figure 18) were tested. Smaller gaps would have resulted in unwanted arcing while larger gaps would not have produced any measurable thrust.

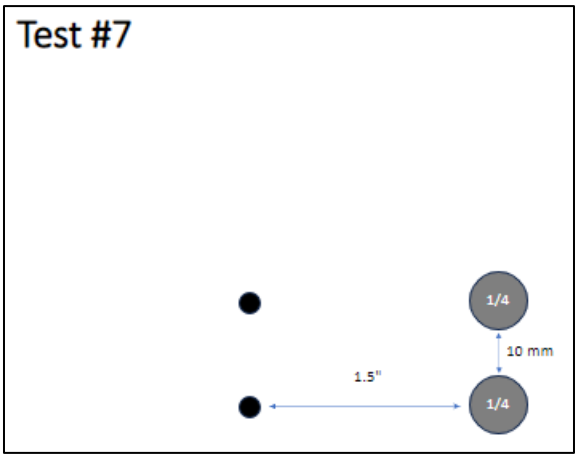

Figure 19: Test Configuration #7

Next, the electrode quantity was varied. For the purposes of this experiment, a comparison was made between using two collector-emitter pairs (Figure 19) versus one collector-emitter pair (Figure 14).

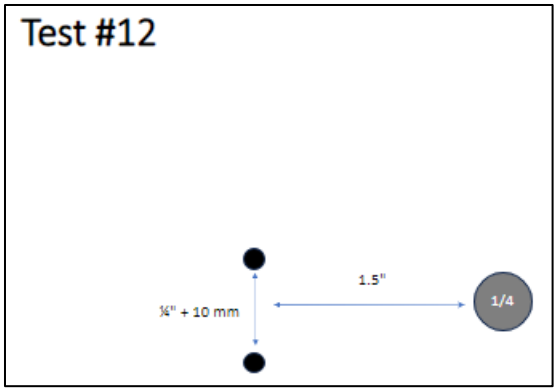

Figure 20: Test Configuration #12

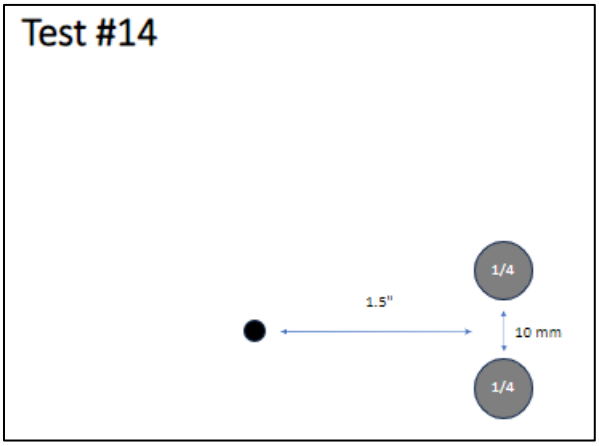

Figure 21: Test Configuration #14

Electrode staggering was also explored. The electrodes can be linear or staggered. For the purposes of this experiment, the team tested using one emitter and two collectors staggered (Figure 21), two emitters and one collector staggered (Figure 20), two emitters and two collectors in line (Figure 19), and one emitter in line with one collector (Figure 14). Other configurations can be tested in future experiments.

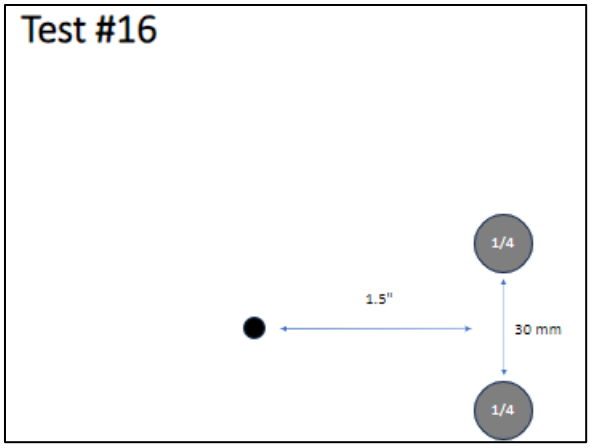

Figure 22: Test Configuration #16

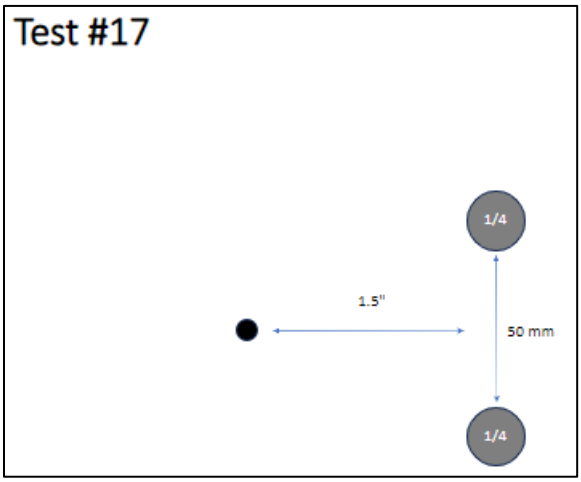

Figure 23: Test Configuration #17

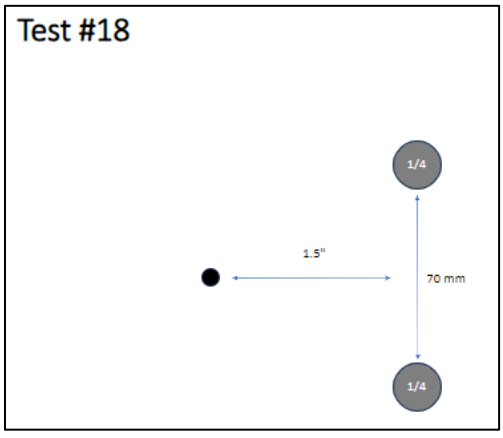

Figure 24: Test Configuration #18

Lastly, the space between the collectors can be varied. For this experiment, collector spacings of 10 (Figure 21), 30 (Figure 22), 50 (Figure 23), and 70 mm (Figure 24) were proposed. Unfortunately, as a result of time constraints, the team was not able to run these tests. However, this parameter can be evaluated in future experiments.

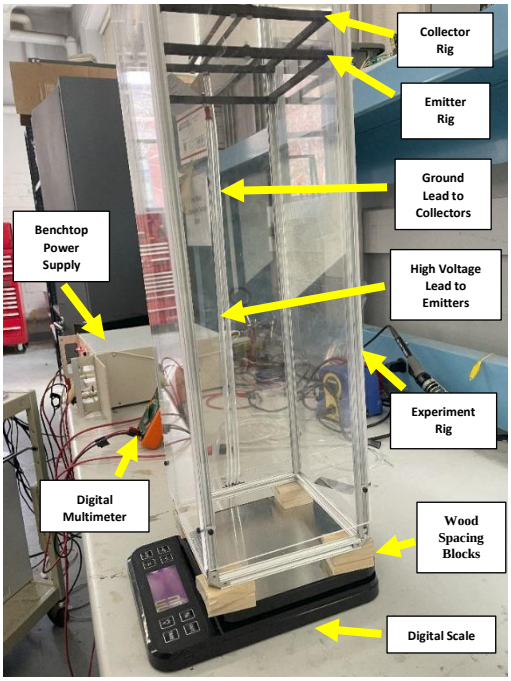

Figure 25: Experiment Setup Diagram

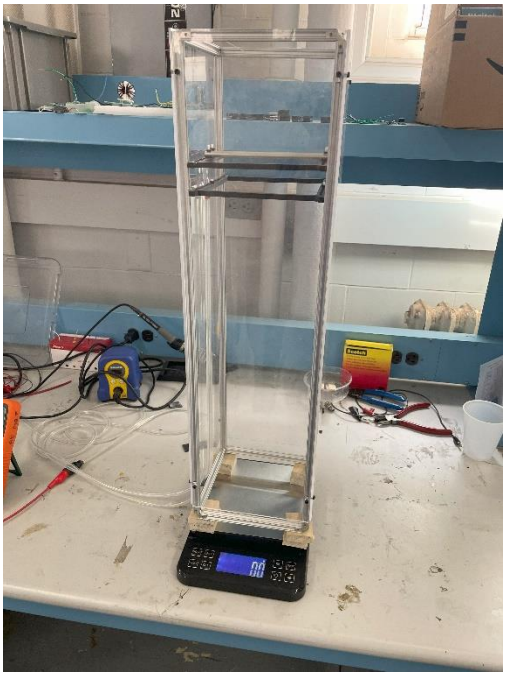

Figure 26: Experiment Rig and Scale

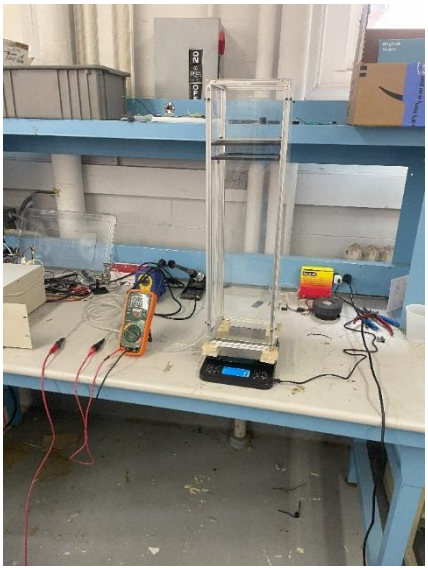

Figure 27: Ionic Wind Experiment Setup with Benchtop Power Supply and Multimeter for Current Monitoring

Figure 25 shows the key components of the experiment setup. A digital scale was used for measuring thrust with a resolution of 0.1 g (Figure 26). Wood spacing blocks were cut and placed between the rig and scale to allow air to flow into the rig. A benchtop power supply was used to provide

the necessary voltage to the rig. A high voltage lead from the power supply was connected to the emitter rig. A ground lead was connected from the collector rig to the power supply. A multimeter was integrated into the circuit to measure the current through the system (Figure 27).

3. Power Subsystem Analysis and Design

3.1 Circuit Design

To produce a high DC voltage range for propulsion testing, upwards of 40kV, three stages are required: a power source in DC, a ZVS driver, and a voltage multiplier to step up an initial voltage from batteries.

Figure 28: 4V to 40V DC Boost Converter (Ebay 2024)

First is the power source, a 40V DC boost converter, as seen above in Figure 28. The converter takes a 12V battery and steps up the voltage to output 40V. This component is purchasable and operates with a current limit of 10A. If put in parallel, two of these boost converters would supply the current output running 5A each. This 40V is required to maximize the output voltage for the ZVS driver, which is a high-frequency oscillator that allows one to take a DC current and drive a transformer with AC current to a desired voltage output.

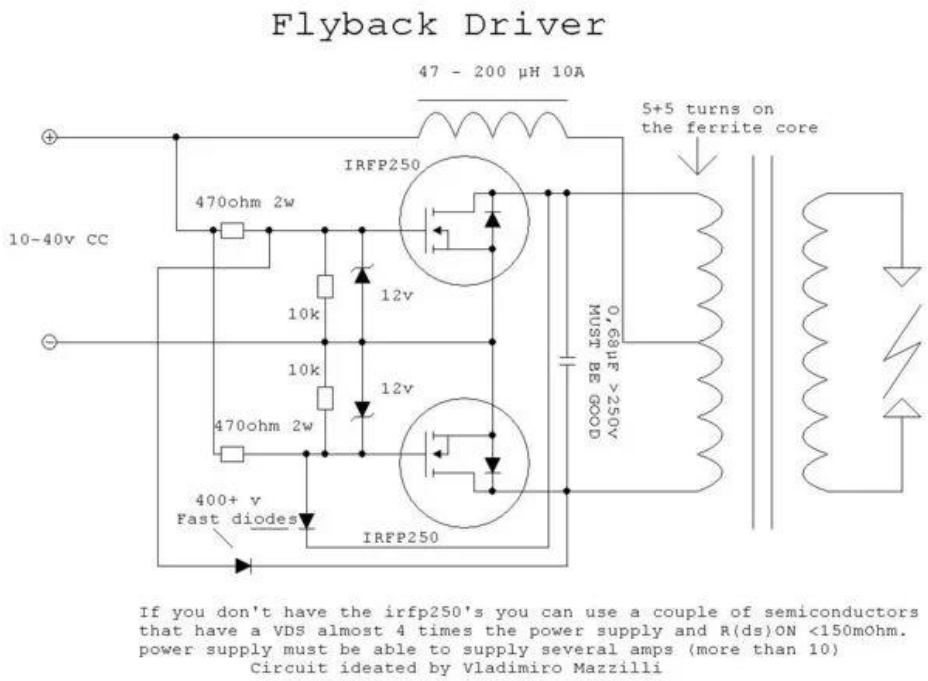

Figure 29: Flyback Driver Circuit Diagram (Tanner_tech 2017)

This ZVS driver is the second stage in the power supply. The circuit designed for this project was modeled off of the circuit above, Figure 29. LTSpice was used to model this ZVS boost circuit as well as the voltage multiplier stages. Due to the ideal operating conditions that LTSpice uses, there is no initial noise in the circuit which is required for the first MOSFET to have enough current to turn off and turn the second MOSFET on. In order to replicate this noise, which happens in normal operating conditions, an impulse current of 0.1 A was added for 1 nanosecond.

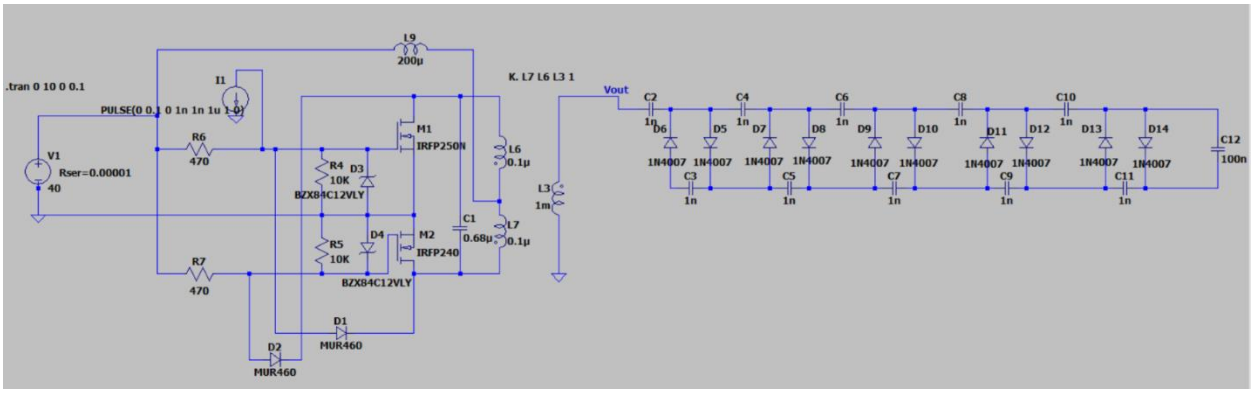

Figure 30: ZVS Driver and 5-Stage Voltage Multiplier Circuit Diagram

First, an inductor, which is labeled L9 on the circuit in Figure 30, is used as a "choke" to limit the amount of current that leads into the transformer. The part purchased for this inductor was a common mode choke, rated for 0.2mH, or 200µH, 250V, and 15A. This inductor can be of a range of inductance from 47µH to 200µH at 10A or higher (Tanner_tech 2017). In order to maximize the voltage output leading into the flyback transformer, the team chose the high end of the needed inductance. If the lower end of the inductance values was chosen, there would be more current which isn't the intended goal. As for the MOSFETs, if it has too high of a current flowing into a gate it will burn out. As the current flows, the inductor causes this choke, called an inductive choke. The current is prevented from having a fast rise time within this inductive choke, since the magnetic field within the inductor builds slowly. The slow rise in current prevents the MOSFETs from getting damaged when switching, the first MOSFET is filled and this controlled current slowly switches to the next MOSFET. The switching of the MOSFETs happens when the first MOSFET's gate-source voltage is larger than the source voltage. One IRFP240N and one IRFP250 MOSFET are used, respectively. In making the transformer, current flows through the inductor on the first top coil, labelled L6, and then through two resistors, R6 and R7, at the gates of each respective MOSFET. The two resistors are there to regulate the current flowing through the gates of the MOSFETs, because if there's too much current, as previously stated, it could damage the MOSFETs. The two 10kΩ resistors each connect a gate of the MOSFETs to ground to prevent parasitic capacitance on the gate, because once they're charged then they might not turn off and they would keep accumulating charge. Two 12V Zener diodes are also used to control what leads into the MOSFETs, where they limit the voltage through a process of voltage tightening so that, even if inputting 40V into the circuit, 12V will always lead into that connected gate of the MOSFET. In order for the oscillation to happen between the MOSFETs, one will fill up with current first due to the imperfections within the circuit. The switch to the second MOSFET doesn't happen until one diode turns on before the other. The noise or imperfections in a circuit, from variations in voltage or current since no two components are perfect, leads to one MOSFET turning on before the other. With current flowing through the first resistor and into the first MOSFET, this MOSFET is turned on, however, the output wire to this MOSFET is grounded. With this

gate grounded, it will shut off current to the second MOSFET, because the flow will go through the second fast diode, D2 in the figure, which leads to the second 470Ω resistor which is in parallel to ground. This causes all the current to flow into the first MOSFET and very little will flow through the second. In the transformer, once the top inductor, L6, draws enough current, a magnetic field will be created around this coil and cause the voltage after the second MOSFET and the 0.68μF capacitor, C1 in the figure, between them to rise and fall. This happens because the capacitor is in parallel resonance with this inductor, which is the frequency where the current is in phase with the voltage (Navi, 2000). Within this parallel resonant circuit, if a small boost of power is given the circuit will start oscillating back and forth. Leading into the top inductor of the transformer, a positive current will be flowing initially, however, when the oscillation starts this point will eventually reach negative or zero current. This is because current will be pulled by the first fast diode, D1, from the first 470Ω resistor, R6, and into the second MOSFET, M2. Ultimately, shutting off the second MOSFET to a ground potential. Since the first resistor R6 is at a positive potential it will flow to ground and stop current flow to the gate leading into the first MOSFET, turning it off. As soon as the first MOSFET turns off, current will flow through the second 470Ω resistor and into the second MOSFET. As soon as the second MOSFET turns on, the second fast diode, D2, will take have all current flow to the second MOSFET and have the first MOSFET be at a ground potential so only the second MOSFET is on. Since current is now flowing from the second MOSFET and into the transformer, the current flow will be in the opposite direction and flowing into the second coil on the transformer, L7 on the diagram. The current will flow from the transformer and into the first MOSFET and its output wire to be positive from current flow and the output wire of the second MOSFET to be ground. This oscillation, or switching of the MOSFETs will continue and push current through the first and second 470Ω resistors. This constant push-pull of current will create a magnetic field that fluctuates inside the transformer and induces current into the secondary coil, L3, of the transformer allowing it to create a high voltage potential from the difference of windings. The input voltage on the primary windings is 345V DC and the output voltage leading into the voltage multiplier is 4.2kV AC.

Most ZVS drivers make use of old TV or street light flyback transformers due to their high current output. Although in this design the team decided to purchase individual materials to create a custom flyback transformer. The voltage a transformer outputs is dependent on the ratio of turns on the primary and secondary cores. For example, if the primary coil has ten turns and the secondary coil has 100 turns the transformer has a turns ratio of 1:10 and the output voltage is ten times the input voltage. With a 345V DC input, the turns ratio is calculated by dividing the desired secondary coil's voltage by the primary coil's voltage. This will be the current transformation ratio where the number of primary windings divided by the number of secondary windings is 0.082. The desired output voltage was desired to be 4.2kV, because the goal of the custom power supply is to get 40kV DC voltage output. Since the voltage multiplier multiplies the input voltage by ten, the input voltage for the voltage multiplier had to be at least 4kV.

This ZVS driver outputs a high current from the voltage and current input starting at 40V DC and 10A, which makes the power 400W. The ZVS driver can also be run at 12V and 5A for a lower voltage output for testing. The two MOSFETs are mounted on heatsinks to dissipate any heat if they're switching at 40V. If the MOSFETs are alternating at zero voltage, they won't get hot, however, if they're switching at 40V, the energy is dissipated as heat.

The final custom circuit component is a 5-stage voltage multiplier. Each of the 5 stages has two capacitors and two diodes in series, where the final stage output voltage will be DC and ten times that of the input AC voltage. In a single stage of a voltage multiplier, the first diode charges the first capacitor to the input voltage from the ZVS driver, which is 4.2kV. The voltage of the first capacitor adds to the input voltage, and through diode 2, the second capacitor is charged to twice this input voltage. Diodes only allow current to flow in one direction. Since the circuit has high voltage, the breakdown voltage of these diodes is very high to ensure that they don't allow current to flow in the opposite direction. Since there are 10 ceramic diodes so as to decrease any potential voltage drop, the power dissipated by each diode can be calculated using $P=IV$. These diodes direct current flow into high voltage capacitors that are charged either negatively or positively on the respective plates of the capacitor. As the charge moves to

each capacitor in parallel, the different voltage that each plate has will keep adding to each successive capacitor so that at the "end" of the circuit the first capacitor in the voltage multiplier will have a voltage of zero. A heatsink is used for the voltage multiplier to decrease losses in energy due to heat. Hollow copper tubes are used, the greater the diameter of the pipe, the greater the heat sinking ability. This five-stage voltage multiplier provides a voltage output of 10x the input voltage.

In parallel with this custom circuit, a second power supply was explored. A Spellman high voltage power supply was tested for its rated 30kV and 300μA, after the replacement of a NIS USB-6008 to a NIS USB-6001 DAQ card. The power supply is a CZE30PN2000, is programmed and monitored by LabView software. The controls monitored by LabView are the control monitor for power and current, the ground fault indicator, GFI, and the indicator for whether the power supply is in voltage or current mode (Cote, 2012). LabView communicates with the DAQ card, data acquisition card, and signals to the Digi Key power supply for the status of the Spellman and the input programmed controls from LabView by its D-Sub 25 connector, where if 24V DC are sent to pins 14 and 1, high voltage is enabled.

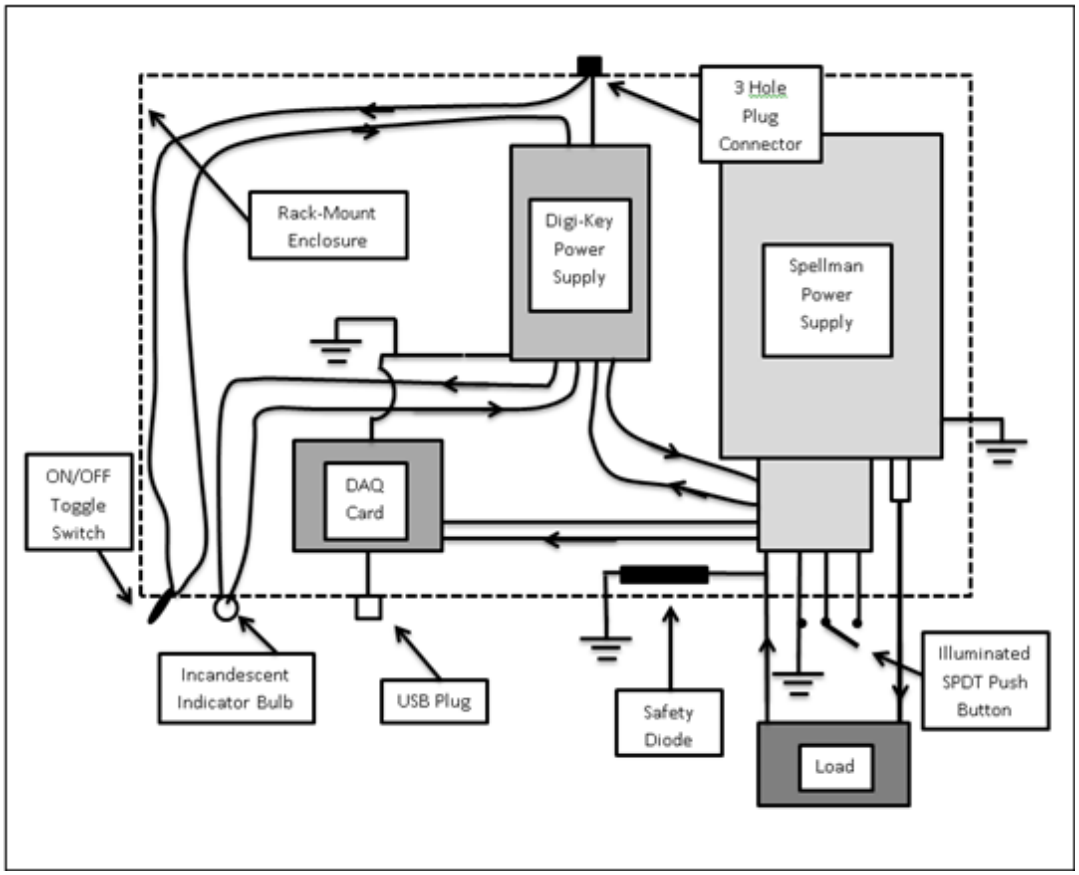

Figure 31: Schematic Wiring Diagram of the Spellman Power Supply (Cote, 2012)

3.2 Component Selection

Selecting components that are both reliable and properly rated for their application is critical for a working and consistent circuit, as well as general safety. When working with such high voltages and power, the ratings and specifications for each component must be thoroughly considered. An additional concern is the size of the components. Most of the passive components are relatively small; however, the overall weight of the entire power supply must be considered for future applications of ionic wind propulsion. Smaller component geometry is also optimal for building a more compact power supply. There are constraints in the design's compactness; for example, when components are too close, it can create issues like parasitic capacitance. These constraints, along with the project budget are the most influencing factors when selecting components. The components were chosen based on parameters used in the LTSpice circuit simulation.

All components of the circuit, aside from the transformer, are mounted on prototype PCB boards. The prototype PCBs were chosen for their ease of construction and mounting and their modularity. The ZVS driver consists of two MOSFETs, four resistors, four diodes, one capacitor, an inductor, and a transformer.

The MOSFETs are both N-channel, requiring a drain to source voltage of 200V, a gate charge of 70nC, and a drain-source on resistance of 0.18 Ohms. Vishay Semiconductors produces a MOSFET that has the above specifications. Since the MOSFETs are the component most likely to overheat in the ZVS driver, a few heat sinks were purchased to help dissipate any heat.

The resistors in the ZVS driver are all metal oxide resistors, and all manufactured by TE Connectivity. Both the 470Ω and the 10kΩ resistors are rated at 200V, which is a conservative rating for the initial portion of the ZVS driver, given there is only a 40V input. The two types of diodes used in the ZVS driver were the MUR460 diodes, and the BZX84C12VLYT116 diodes, manufactured by Diotec Semiconductor and Rohm Semiconductor, respectively. The MUR460 diodes are silicon diodes that have a breakdown voltage of 600V, and an average forward current of 4A. The BZX84C12VLYT116 diode is a Zener diode and has a breakdown of 12V.

The capacitor in the ZVS driver has a capacitance of 68 μF, and is rated for 400 V. This capacitor is an aluminum electrolytic capacitor and is manufactured by Cermant. The inductor that was selected is manufactured by KEMET and was chosen for its inductance of 200 μH and rated current of 15A, and additionally for its compact size relative to other similar inductors.

The transformer is necessary for stepping up the DC output voltage from the ZVS to a much higher AC voltage to enter the voltage multiplier. The turns ratio between the primary and secondary windings determines the factor that the voltage will be multiplied by, which needs to be 1:13. The first winding must be rated between 300-400 VDC, while the secondary winding must be rated at 4.2kV. Because there are few commercial off-the-shelf options both available and within budget for a transformer with these specifications, building a custom transformer was favorable.

To build the transformer, two types of wire were required, one for the primary winding, and one for the secondary. A 16-gauge copper wire was used for the primary winding. Since a large current, around 500 A, was expected to flow through the secondary windings, a 4-gauge copper wire was chosen for the secondary. These windings were wrapped around opposing sides of a ferrite core to form the transformer.

The final portion of the circuit, the five-stage voltage multiplier, is comprised of twelve capacitors and ten diodes. This portion of the circuit is where the highest voltage is produced. Through research of similar voltage multipliers, it was found that most experiments used capacitors that were rated for voltages ranging from 10 to 20kV (He, Yiou et al, 2017). Ceramic, mica, and film capacitors most commonly fulfill this requirement. Ultimately, a ceramic capacitor was chosen over the other options due to its optimal tradeoff in the voltage rating and capacitance. The ceramic capacitors are also much smaller and lighter in weight. With these requirements in mind and the budget constraints, high voltage disc ceramic capacitors manufactured by Vikye were selected.

Through simulation of the voltage multiplier in LTSpice, it was found that the highest priority specifications for the diodes were a breakdown voltage of 10kV and an average forward current of 1A. The DD1000 diode from Diotec Semiconductor satisfies these requirements and offers the benefit of a quick reverse recovery time, ~1500ns.

The above passive components for the ZVS driver and voltage multiplier meet the requirements and inputs outlined by the LTSpice circuit simulation. However, through additional research, advantages of other specifications, such as material were found, to improve the overall performance of the circuit and reduce complications for building and testing.

4. Findings, Analysis, and Future Recommendations

4.1 Wiring and Calibrating the Spellman Power Supply

The power supply was initially tested and calibrated using a simple circuit, consisting only of a 1GΩ resistor, as shown in Figure 32. The high voltage output of the Spellman was connected to one end of the resistor on a PCB board, while the negative end of the resistor was connected to the positive probe of an ammeter. The negative probe of the ammeter was connected to the common terminal on the power supply. To measure voltage, a high voltage probe was used on the positive side of the resistor. This probe stepped down the voltage by a factor of 1000 to provide a reading on a voltmeter. The negative lead of the voltmeter was also connected to the return on the power supply. Lastly, the circuit was grounded by connecting the common terminal to the metal chassis of the power supply.

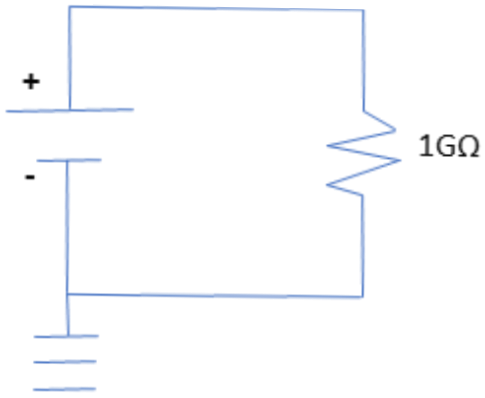

Figure 32: Schematic of circuit used for initial calibration

Before conducting any testing with the propulsion system, the Spellman power supply was calibrated. During the first attempt at calibration, it was determined that the power supply was only capable of outputting a maximum of 15kV. While the Spellman power supply is rated to output a maximum of 30 kV, the NI-6008 DAQ card that serves as an intermediate between the LabVIEW VI and the power supply is only capable of a 5V output. To achieve a 30 kV output on the Spellman power supply, an output of 10V from the DAQ card is required. To address this, a new DAQ card was purchased

to replace the NI-6001. The NI-6001 was chosen since it fulfilled the requirement of having a 10V output rating.

Calibration was continued once the DAQ card was replaced. Beginning with a 1 kV voltage control input in the LabVIEW VI, readings on the voltmeter, ammeter, voltage monitor panel, and current monitor panel were recorded. Ten voltage control inputs were tested, in increments of 1kV, with the highest voltage being 10 kV. To create the calibration curves shown below, the voltage control values were scaled to fit on a 0-10V scale. Three curves were created; the voltage control and voltage monitor were graphed against the voltmeter readings, and the current monitor was graphed against the ammeter readings. The slopes and intercepts obtained from the trendlines of these curves were used as inputs in the LabVIEW VI block diagram, as shown in Figure 33 and Figure 34.

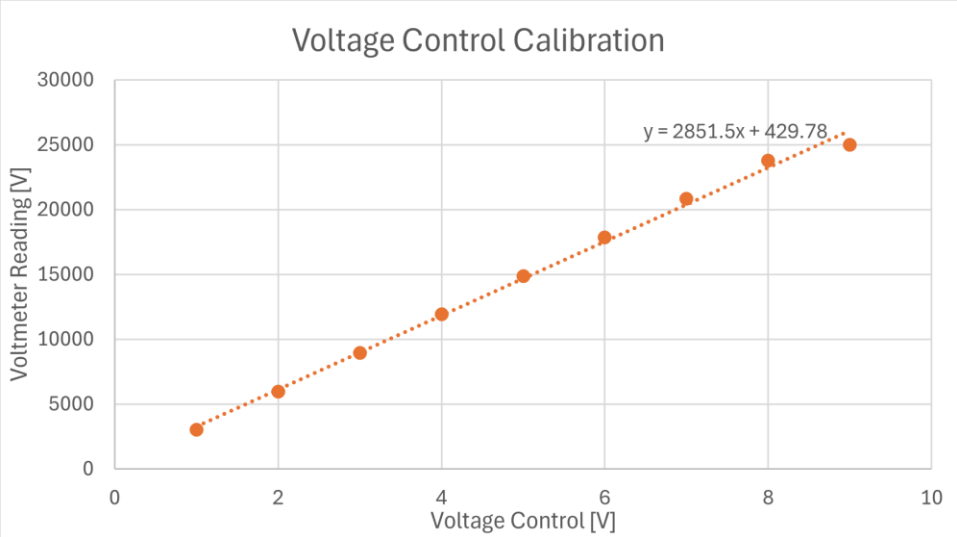

Figure 33: The calibration curve for voltage control

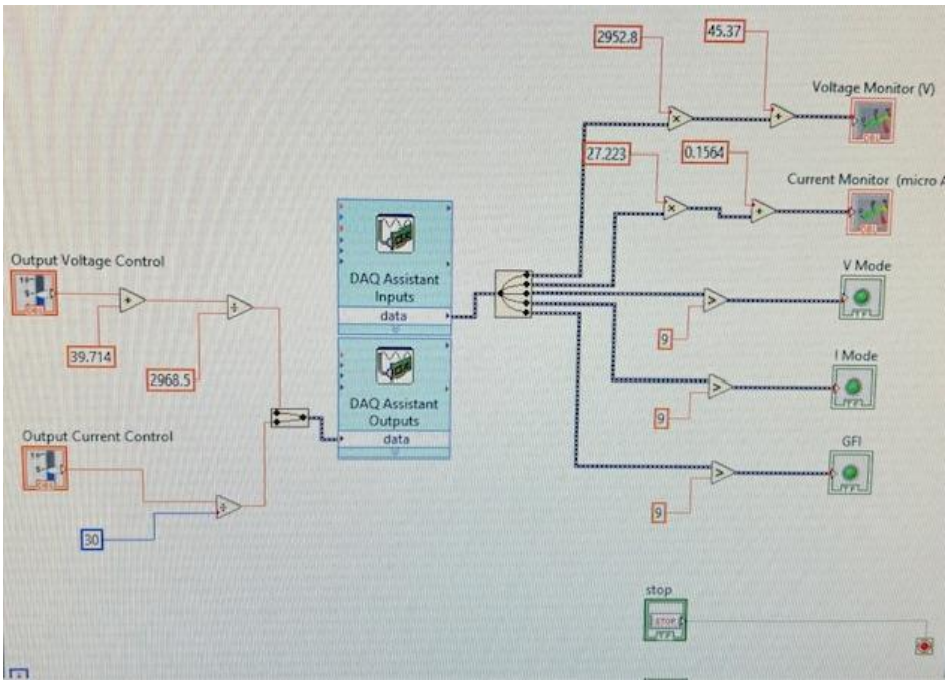

Figure 34: Block diagram containing the slopes and intercepts from the calibration curves

Table 3: Calibration Results

Voltage Control [V]	Voltage Monitor [V]	Current Monitor [µA]	Voltmeter Reading [V]	Ammeter Reading [µA]
1000	1	1.10	3017	30.1
2000	2.01	2.21	5970	60.3
3000	3.04	3.32	8940	90.7
4000	3.98	4.45	11910	121.5
5000	5.04	5.62	14890	152.6
6000	6.03	6.74	17850	183.9
7000	7.04	7.98	20820	215.8
8000	8.05	10.9	23790	250

During calibration, arcing began to occur between the two leads of the resistor at about 7 kV. To accommodate for this, the PCB board was potted in a container of epoxy, shown in Figure 35 to prevent electricity from jumping from leads. After the epoxy had fully cured, there was no longer any arcing, however, the epoxy felt warm at voltages above 10 kV.

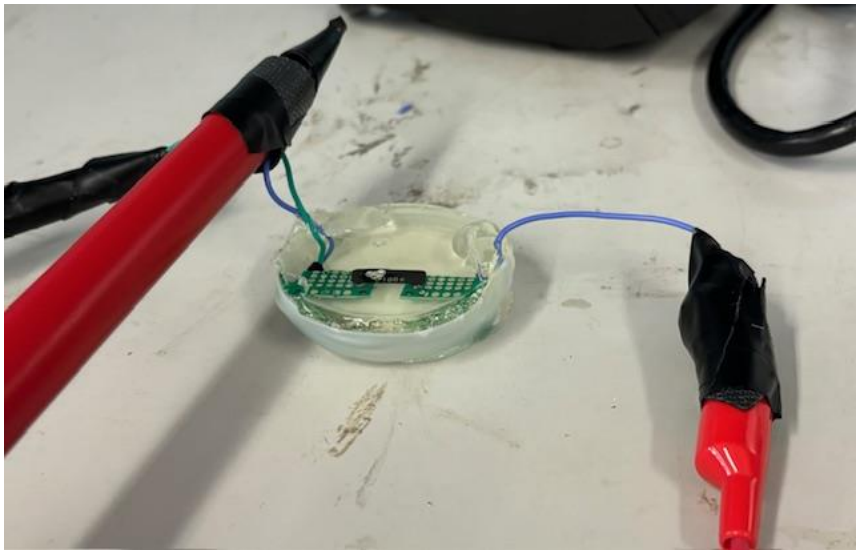

Figure 35: The PCB board and resistor were potted in a small container of epoxy to prevent arcing

The power supply was determined to be safe and reliable working with voltages up to 25 kV. At voltages above 25 kV, there were charges that could be heard near the common terminal, indicating a possibility of arcing at higher voltages.

4.2 Experimental Testing with the Spellman Power Supply

For the propulsion system experimental setup, the high voltage output of the power supply was connected to the emitter wire. The collector wire was connected to the positive lead of the ammeter, and the negative lead of the ammeter was connected to the common port. No resistor was used in the experimental setup. All exposed connections were wrapped in high voltage electrical tape to prevent arcing and for safety reasons. Since the power supply was calibrated, it was not necessary to measure the voltage output. However, measuring the current was a critical step in the experiment, as it is used as an indicator of a closed circuit, and thus a corona discharge.

4.3 Construction and Testing of ZVS Driver

The tools used to make the ZVS driver were a soldering iron, two PCB boards, wire cutters, wire strippers, electrical tape, soldering wick, and small mounting arms. Working from left to right, the design schematic of the custom circuit on LTSpice was followed as the layout for the PCB board. Components

were bent into the board and then soldered with necessary wires soldered to them if necessary to reach the next component. On a separate small PCB board, the 200µH inductor is wired and soldered in series with the initial power source, for testing the team used a 30V power supply. On a larger PCB board the majority of the components are laid out, first, the 470Ω resistors were added in parallel to the power supply. Next, the MUR460 diodes are soldered in series to these resistors and wires are soldered to give them the reach to their respective gates on opposite MOSFETs to their placement on the board. Next, the 470Ω resistors are soldered to two 10kΩ resistors, which are then soldered in parallel to two Zener diodes, with the part number BZX84C12VLY. The wire leading into the 10kΩ resistor and the Zener diodes from the 470Ω resistor has a wire soldered to lead into the first gate of the MOSFET, furthest left. The wire connecting the flow after the 10kΩ resistor and the Zener diode is led from ground on the left most part of the circuit, through these connected four components, and to the middle gate of the respective MOSFET. Heatsinks were glued to the bottom of each MOSFET and allowed to dry overnight because these components are known to heat up from the oscillation that happens as their gate-source voltage is reached by the source voltage. The MOSFETS have three gates, the furthest right one being their output voltage. The IRFP250N MOSFET is soldered to the top-most part of the PCB board and the IRFP240 MOSFET is soldered to the bottom right of the board. Finally, the output voltage from the right-most gates of these MOSFETS is soldered to the 0.68µF capacitor in parallel. Components are checked for cold connections by checking the solder, a shiny solder means the components were soldered well. By heating up the area to be soldered first, the solder will be able to melt and connect the joints properly.

Figure 36: Testing Configuration of the ZVS Driver

Finally, testing is done using a 30V power supply. Connections from the lead into the 470Ω resistors are connected using gator clips to banana plugs to the power supply. The circuit is measured using a multimeter from the red probe taped to check the voltage output on the output at the 0.68µF capacitor. The circuit is grounded using both a red gator clip back into a banana plug lead into the power supply, as well as from the white gator clip connected to the back of the power supply.

4.4 Construction and Testing of Voltage Multiplier

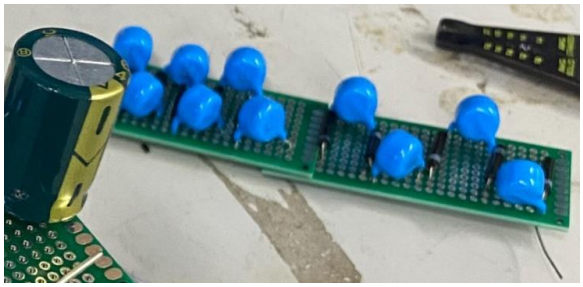

Figure 37: Five Stage Voltage Multiplier Circuit

The tools used to make the five-stage voltage multiplier were a soldering iron, two same sized PCB boards, wire cutters, wire strippers, electrical tape, soldering wick, and small mounting arms. First 10 20kV, 0.001 µF capacitors and 10 20kV high voltage diodes are arranged on a PCB board to make the five stages. Two PCB boards are used since the voltage multiplier is a long circuit. Each component is soldered, with the first component, a 0.001µF capacitor soldered to a 20kV high voltage diode in series, which is soldered to another 0.001µF capacitor in series, which is soldered to another 20kV high voltage diode, etc. The process is repeated until the boards are connected and the output voltage is after the tenth 20kV high voltage diode. Due to the high voltage in this circuit, epoxy was used to coat the solder joints below the PCB board. This is done to prevent arcing. In order to test the voltage multiplier an AC input voltage of just over 4kV is used in the LTSpice model to output the 40kV originally desired. However, for testing purposes, an input voltage of 10V AC will be used to test the voltage multiplier.

4.5 COMSOL Results and Discussion

Simulation 1: The wire electrode radius is 0.2032 mm, the collector electrode is 0.25 in, and the electrode gap is set to 20 mm. The electrode pairs were set to the same height, and the voltage applied ranged from 27 to 30 kV. The simulation results are shown below. The model has a linear trend whereas the voltage decreases, the velocity and thrust also decreases. This acts as expected, since if the system is given less power, then it will produce less force. The velocity simulated is comparable to Huang and Chen where they also simulated a velocity of 3 to 4 m/s with their simulations.

Table 4: Simulation 1 Results

Voltage [kV]	Velocity Magnitude [m/s]	Space Charge Density [C/m^3]	Thrust Density [N/m^3]
30	3.633	3.06E-05	20.091
29	3.4853	2.88E-05	18.418
28	3.3466	2.70E-05	16.828

a)

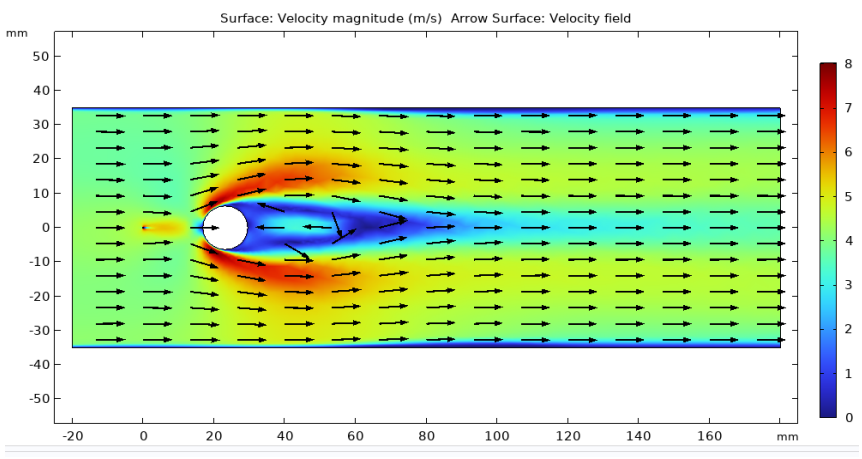

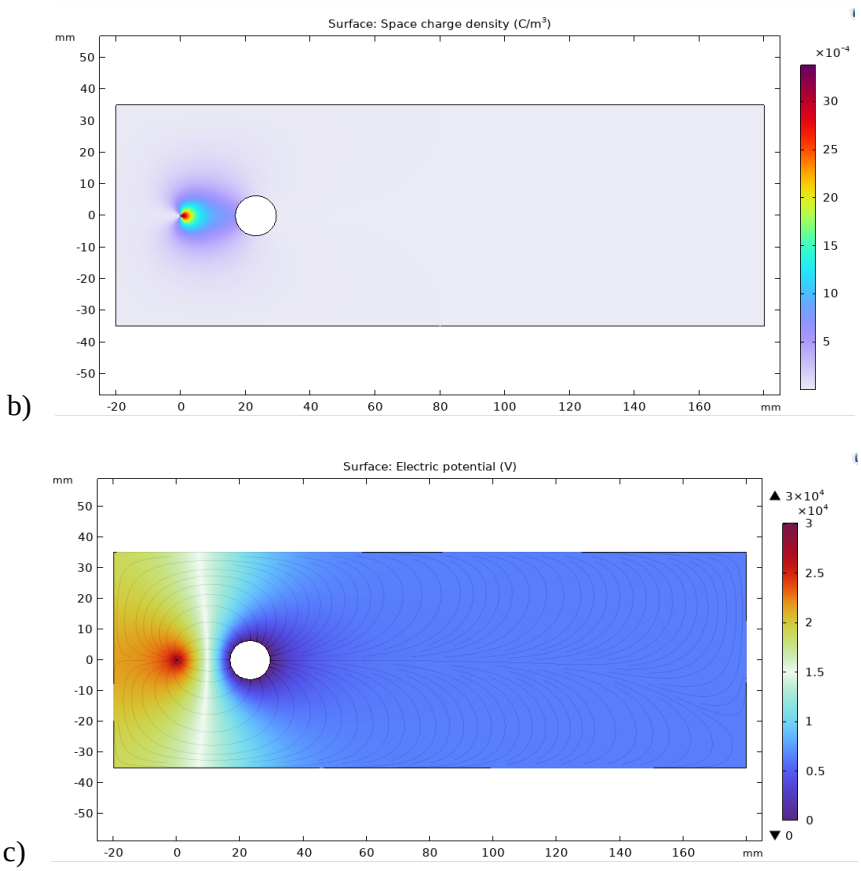

Figure 38: Simulation 1 a) Surface Velocity Magnitude Plot, b) Surface Space Charge Density Plot and c) Electric Potential Plot

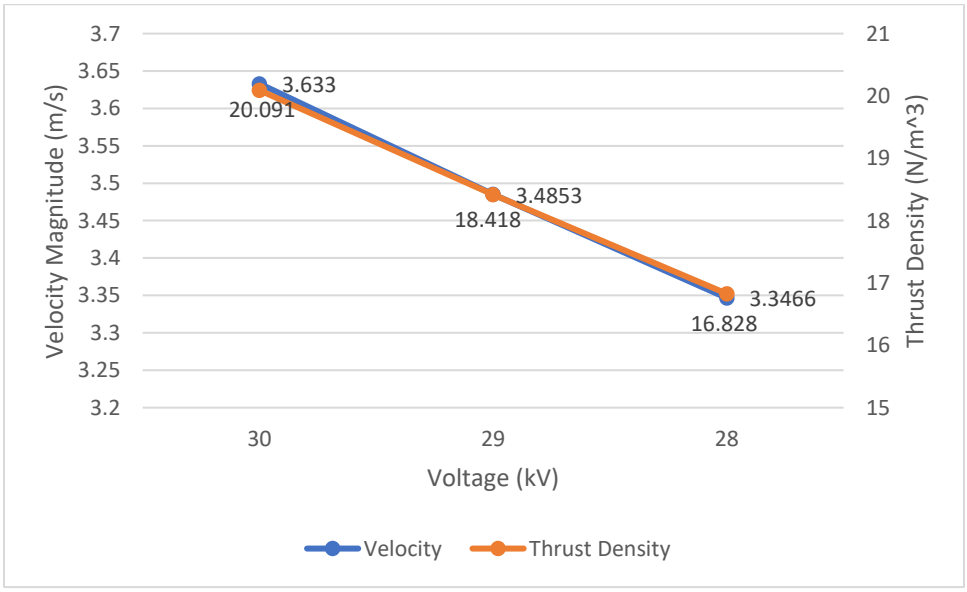

Figure 39: Simulation 1 Voltage vs Velocity Magnitude & Thrust Density (x-direction)

Simulation 2: For this Simulation, the wire electrode radius is 0.2032 mm, the collector electrode radius is 0.25 in, the voltage applied is 30 kV, and the electrode pairs are at the same height. The electrode gap ranges from 14 to 20 mm. The results are shown below. In the second simulation, as the electrode gap decreased, the velocity and thrust force increased. This is because the attraction force of the ion collector is stronger since it is closer to the emitter. The ions are then accelerated more quickly causing an increase in momentum transfer to the neutral ions which gives more thrust.

Table 5: Simulation 2 Results

Electrode Gap [mm]	Velocity Magnitude [m/s]	Space Charge Density [C/m^3]	Thrust Density [N/m^3]
20	3.633	3.06E-05	20.091
17	3.9799	3.42E-05	25.581
14	4.445	3.83E-05	34.131

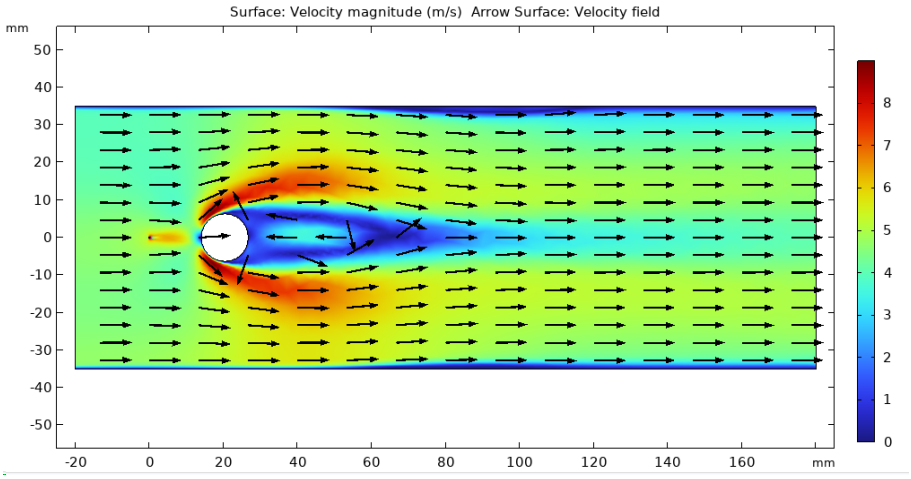

Figure 40: Simulation 2 Surface Velocity Plot at 20 mm Electrode Gap

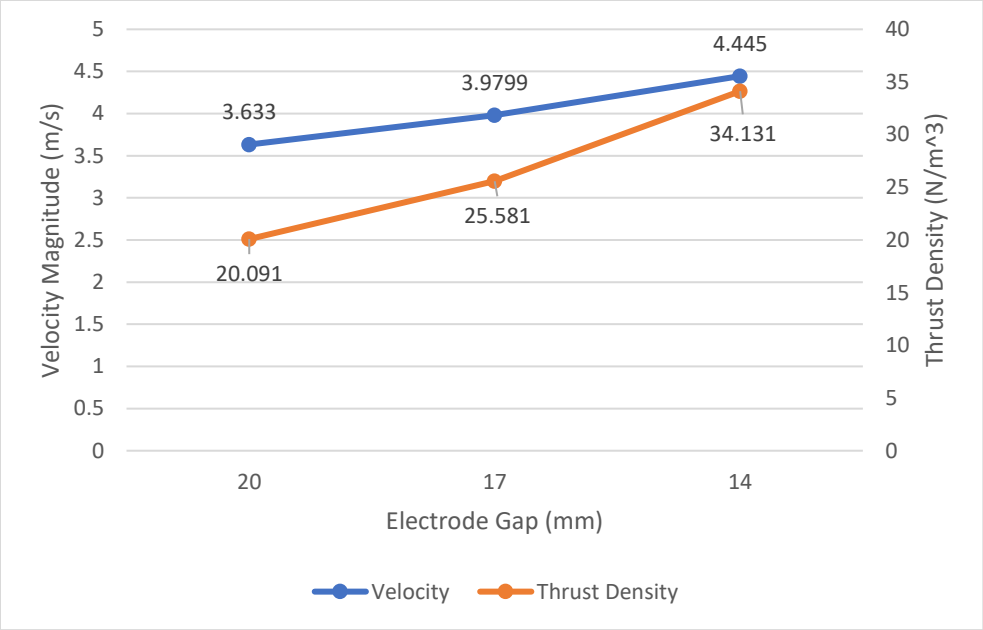

Figure 41: Experiment 2 Electrode Gap vs Velocity Magnitude & Thrust Density (x-direction)

Simulation 3: For this simulation, the voltage was set at 30 kV and the electrode gap was set at 20 mm. The collector radius ranged from 0.225 to 0.25 in. The results are shown below. The model was particularly sensitive to changes in collector radius, so only a range of 0.025 in could be tested. The results may not be significant since the size is so small. However, the results were unexpected. At 0.237 in, the velocity magnitude increased, while the space charge density and thrust density decreased. At 0.225 in, the space charge density and volume force increased, yet the velocity decreased while still being greater than the velocity at 0.25 in. From the other simulations, an increase in space charge density and thrust density causes a higher velocity magnitude, yet the opposite result is shown. There could be an ideal electrode radius depending on the electric potential and electrode gap due to drag on the cylinder. However, more thrust is produced from the larger collector size, suggesting that the ions are accelerated more quickly past the collector to the end of the domain. The model was unable to converge on different size collector radius to further test this simulation.

Table 6: Simulation 3 Results

Collector Radius [in]	Velocity Magnitude [m/s]	Space Charge Density [C/m^3]	Thrust Density [N/m^3]
0.225	3.7025	3.00E-05	19.684
0.237	3.8503	2.95E-05	19.248
0.25	3.633	3.06E-05	20.091

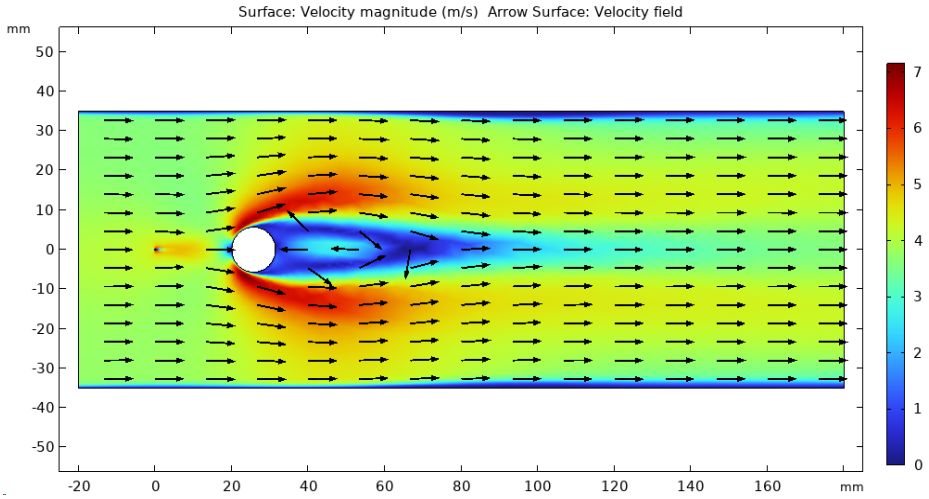

Figure 42: Experiment 3 Surface Velocity Plot for 0.225 in Collector Radius

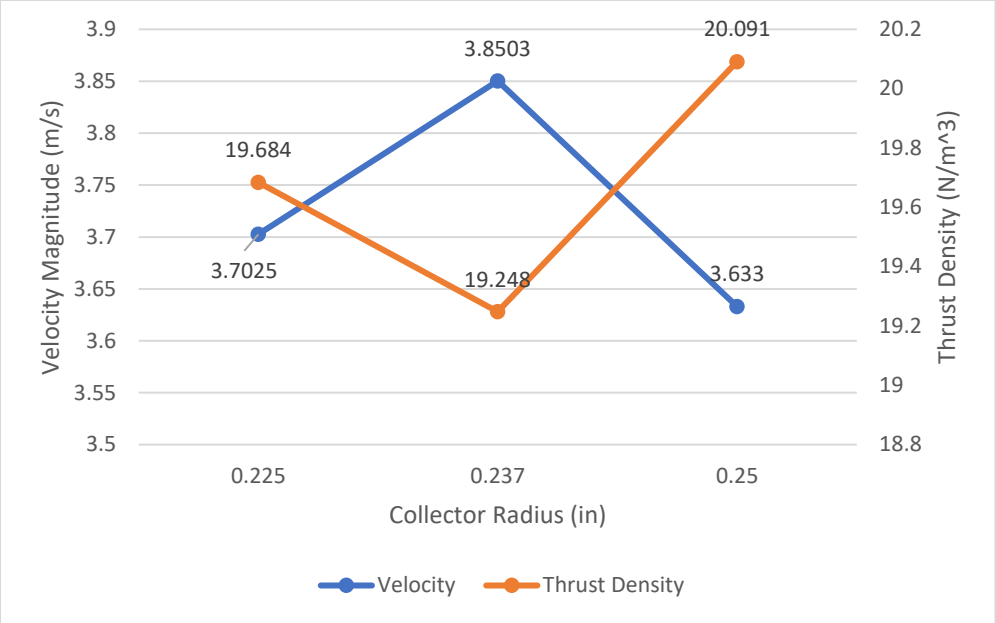

Figure 43: Simulation 3 Collector Radius vs Velocity Magnitude & Thrust Density (x-direction)

Simulation 4: For this simulation, two equidistant collector electrodes were used of radius 0.125 in due to the model not converging for larger radii. Only one emitter wire was used while the voltage was 30 kV, and the electrode gap was 20 mm. The collector gap ranged from 15 to 45 mm. The results are shown below. In the simulation, there was a significant increase in velocity and thrust when using multiple collectors, even when the radius was significantly reduced. It is clearly beneficial to use multiple collectors. The smallest collector gap produced the most thrust. This is because the thrust is measured in the x-direction, so the ions are traveling more linearly than diagonally. Even though the velocity magnitude is faster with a 30 mm gap, the ions are not producing as much thrust since they are traveling diagonally. A sharp decrease in velocity and thrust is displayed for the 45 mm gap since the collectors are farther away from the emitter, and the angle is much steeper.

Table 7: Simulation 4 Results

Collector Gap [mm]	Velocity Magnitude [m/s]	Space Charge Density [C/m^3]	Thrust Density [N/m^3]
15	4.3176	3.52E-05	23.888
30	4.3826	3.89E-05	20.45
45	3.6716	3.78E-05	13.63

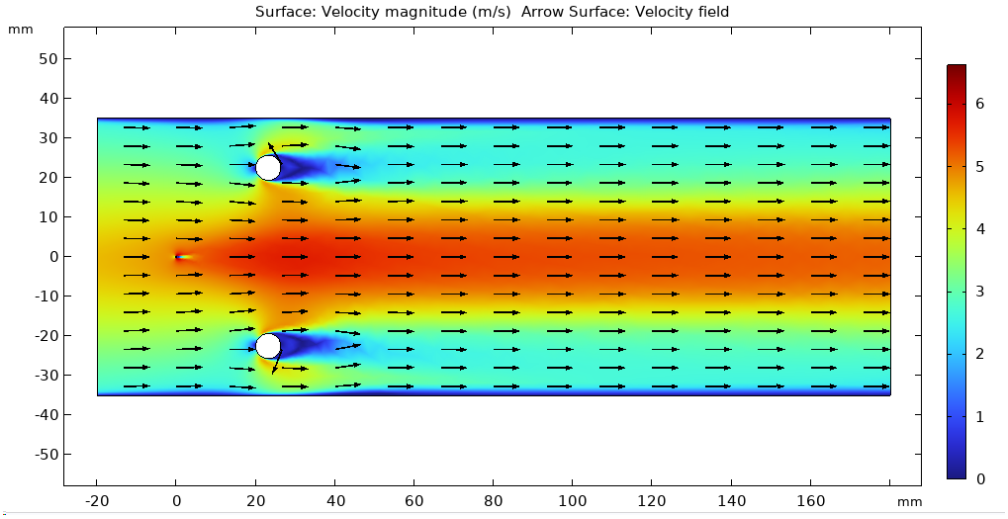

Figure 44: Simulation 4 Surface Velocity Plot for 45 mm Collector Gap

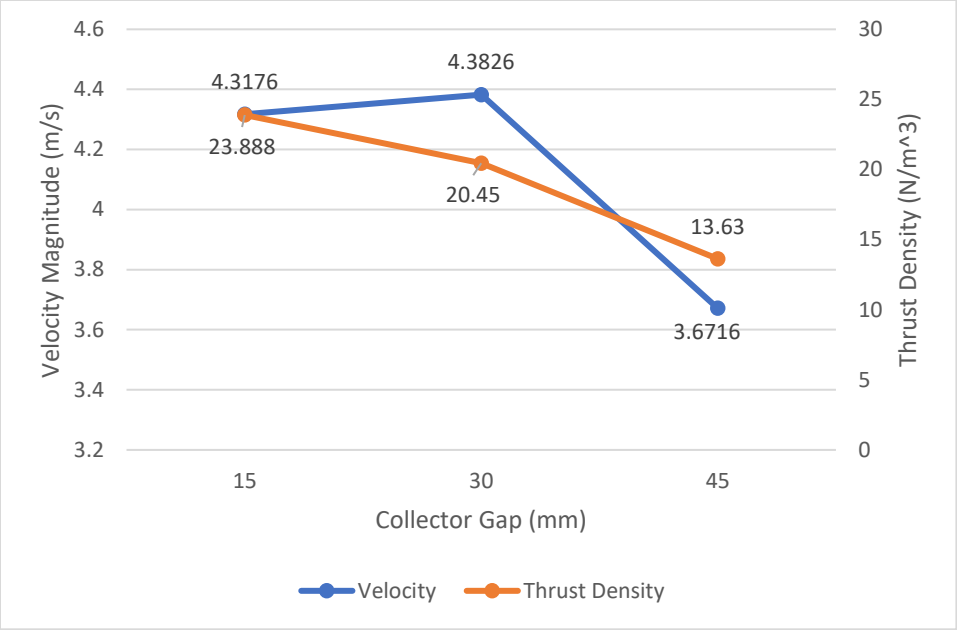

Figure 45: Simulation 4 Collector Gap vs Velocity Magnitude & Thrust Density (x-direction)

Simulation 5: For the final experiment, the model was tested at 30 kV with an electrode gap of 20 mm. However, the model would not converge when using two collectors at 0.25 in radius, but it managed to converge with a 0.125 radius. The model also would not converge with one collector at 0.125 radius. It is evident that with more collectors, the thrust density increases. This is because there are more collectors to attract ions and accelerate the flow in the x-direction.

Table 8: Simulation 5 Results

Collector Quantity	Velocity Magnitude [m/s]	Space Charge Density [C/m^3]	Thrust Density [N/m^3]
1	3.633	3.06E-05	20.091
2	4.3176	3.52E-05	23.888
3	3.6051	4.18E-05	28.486

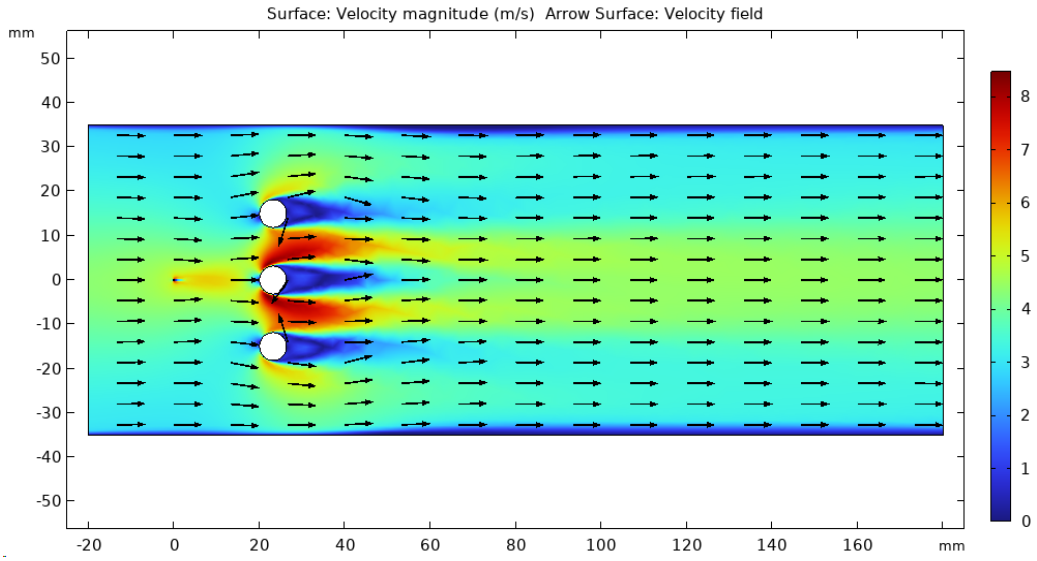

Figure 46: Simulation 5 Surface Velocity Plot with 3 Collector Electrodes

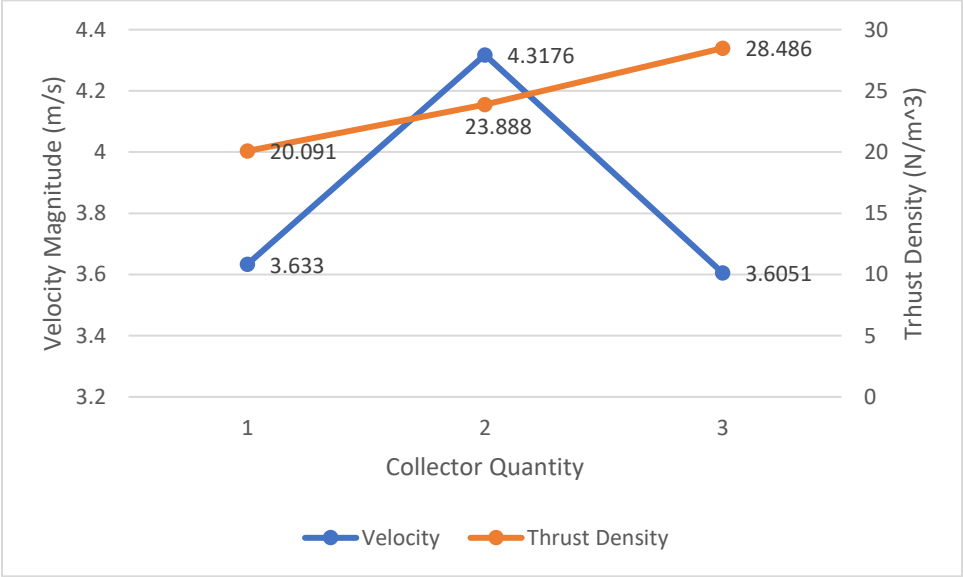

Figure 47: Simulation 5 Collector Quantity vs Velocity Magnitude & Thrust Density (x-direction)

4.6 Future Recommendations for the COMSOL Model

For the COMSOL model, the biggest recommendation is to only simulate half the domain, then mirror the results to show the full domain. This will effectively half the computation time and would allow the model to converge for a far greater range of tests. If it works, then the team could potentially

simulate exactly what has been created in the physical experiments. The domain would be changed to the physical size of the case from the experiment, and the electrode setups would match what was physically tested. With this, the simulations could be compared to the experimental data.

The biggest challenge while creating the simulation was making it converge. The team failed to make the model converge with accurate results. Most of the errors said it could not solve all the degree of freedoms in the model or it exceeded the number of tries to solve below the tolerance of 0.0001. When the model did converge into a solution, the flow was nonsensical and did not accurately model ionic wind results from other simulations. With the help of the COMSOL support team, they were able to make the model converge with accurate results by giving advice on nonlinear equation numerical solving method described above.

While the model was able to successfully converge and have accurate data, it was sensitive to little changes. For example, in simulation 1, the model would not converge for voltages greater than 30 or lower than 28 kV. Many initial parameters were changed to help the model converge but was unsuccessful.

4.7 Ionic Wind Experiment Results

4.7.1 Thrust Density

For comparing the results of the ionic wind experiment to other literature, a common metric for comparison is necessary. Total thrust is an insufficient measurement for comparison since it does not consider the cross section in which the thrust is produced. In a review of existing literature, the common metric for comparing ionic wind propulsion systems is known as “thrust density” which is the total thrust produced divided by the total collector length and has units of $\frac{mN}{m}$. As more collectors are added, the total length increases.

4.7.2 Findings and Trend Analysis

Experimental thrust and current values were recorded for each test at voltages between 0 and 25 kV. These thrust and current values were then plotted versus voltage and a cubic polynomial curve was fitted to each plot. Figure 48 illustrates a thrust measurement of 5.0 grams taken at 25 kV during Test #3. This was the highest thrust value measured during the experiments. This value corresponds to a thrust density of 321.74 $\frac{mN}{m}$ since 49 mN of thrust was produced using one 6 inch collector.

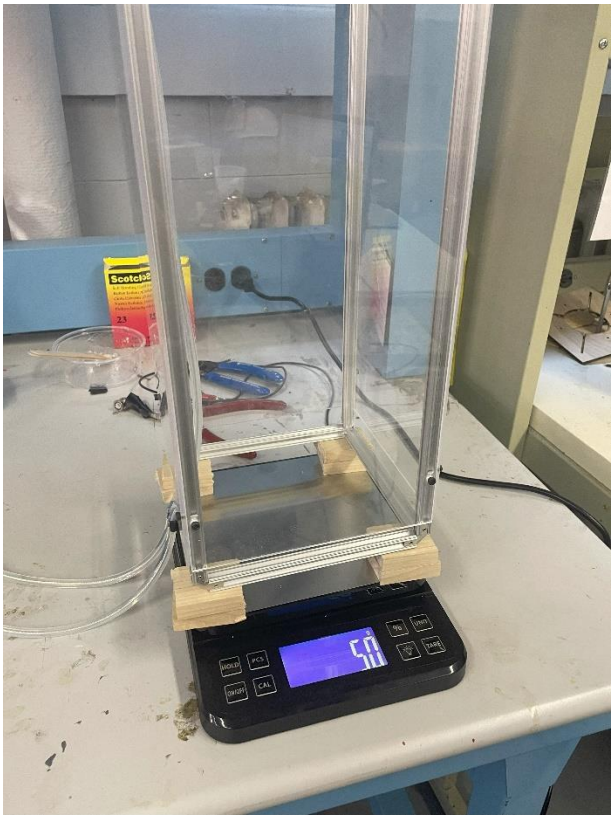

Figure 48: Measurement of 5.0 grams of Thrust at 25 KV for Test #3

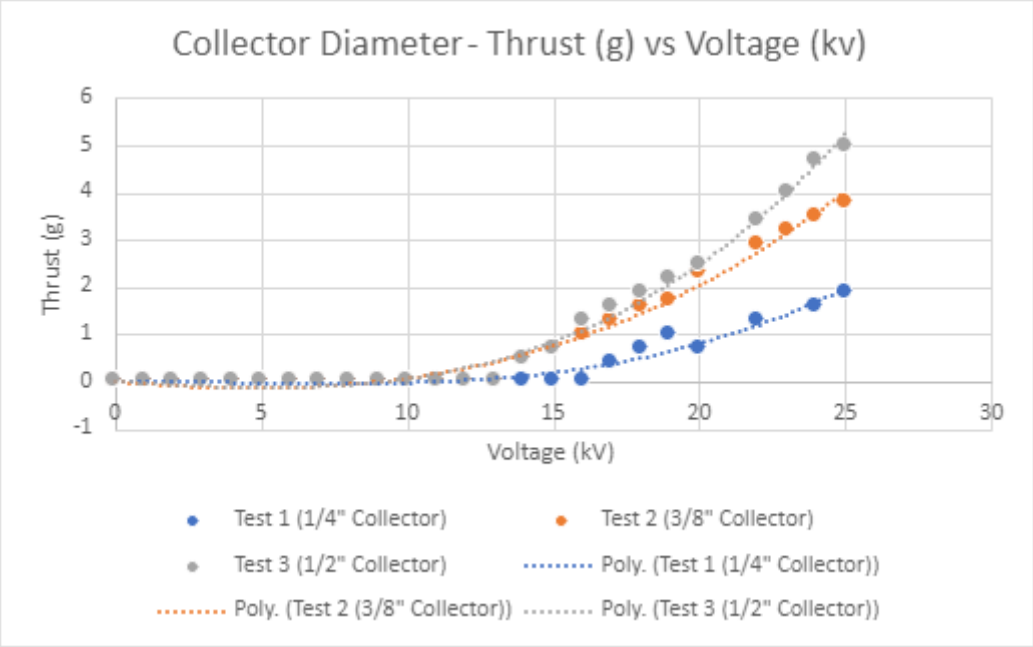

Figure 49: Thrust (g) vs Voltage (kV) for Different Collector Diameters

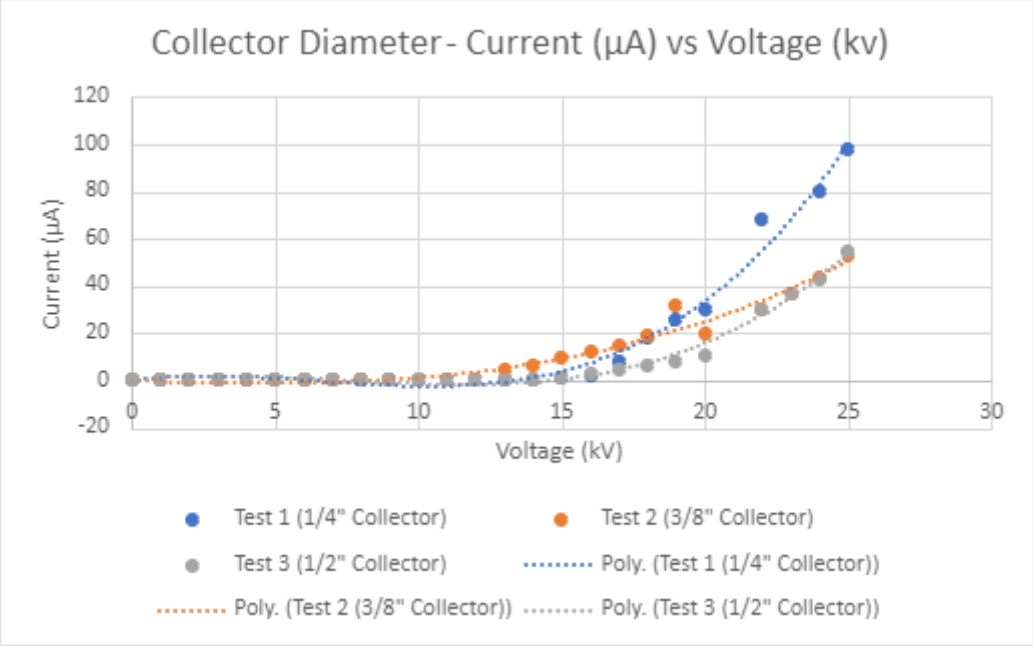

Figure 50: Current (µA) vs Voltage (kV) for Different Collector Diameters

As shown in Figure 49, increasing collector diameter increases thrust. Figure 50 shows that increasing collector diameter decreases the current measured by the multimeter.

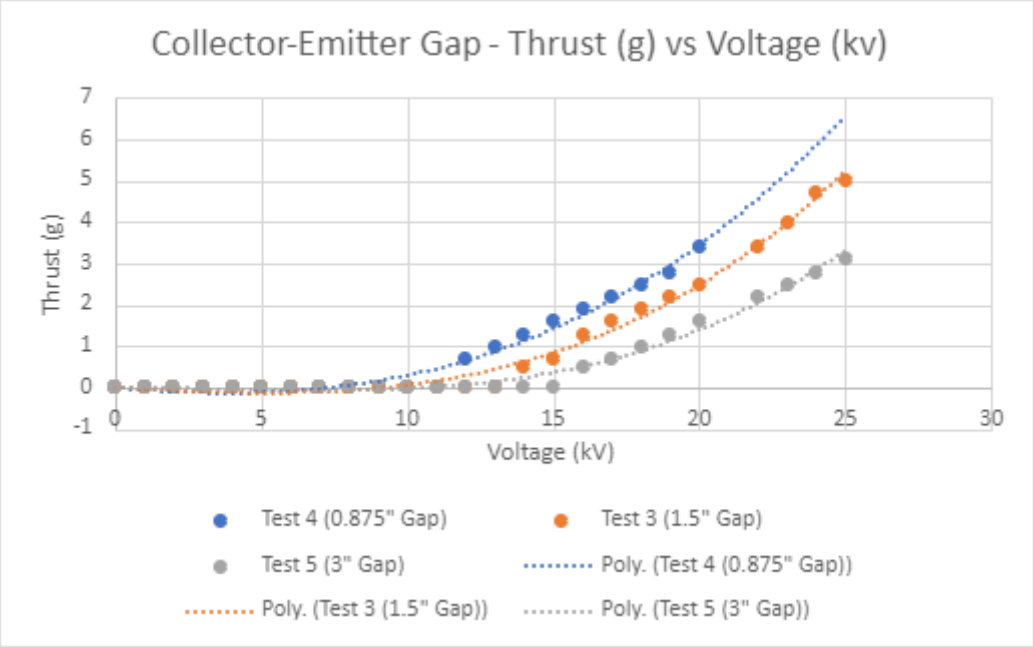

Figure 51: Thrust (g) vs Voltage (kV) for Different Collector-Emitter Gaps

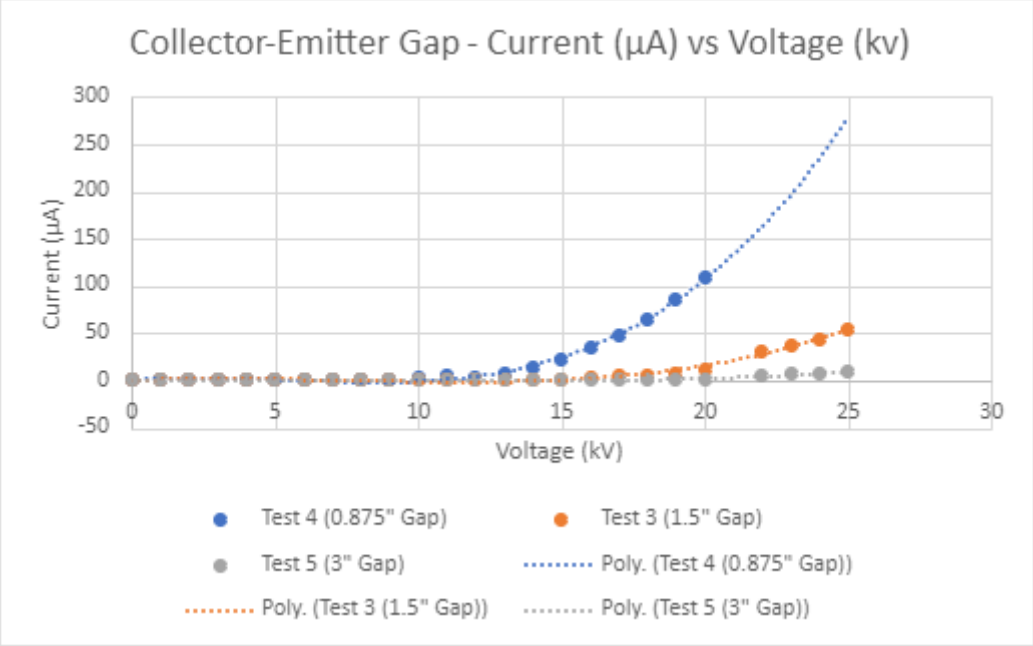

Figure 52: Current (µA) vs Voltage (kV) for Different Collector-Emitter Gaps

As shown in Figure 51, decreasing the collector-emitter gap increases thrust. However, the gap can only be decreased to a certain point. At about 21 kV, the 0.875 inch gap configuration began

exhibiting arcing between the emitter and collector. This is why there are data points missing for 21-25 kV for this gap in Figure 51. Figure 52 shows that decreasing the collector-emitter gap increases the current measured by the multimeter. Both the thrust and the current plots seem to follow a cubic pattern when fitting a polynomial to the curves.

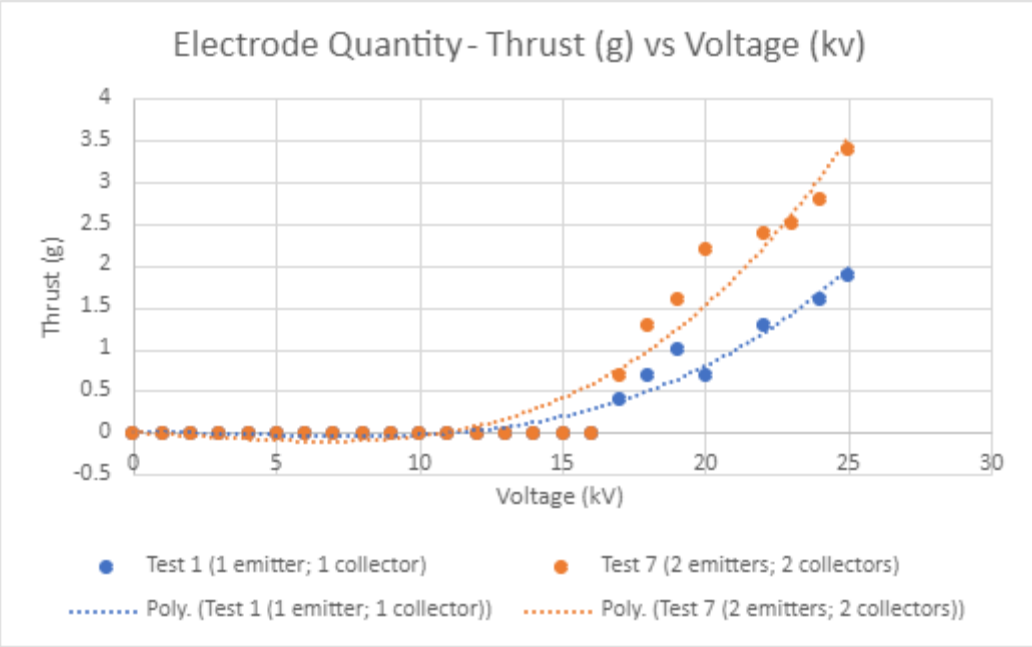

Figure 53: Thrust (g) vs Voltage (kV) for Different Electrode Quantities

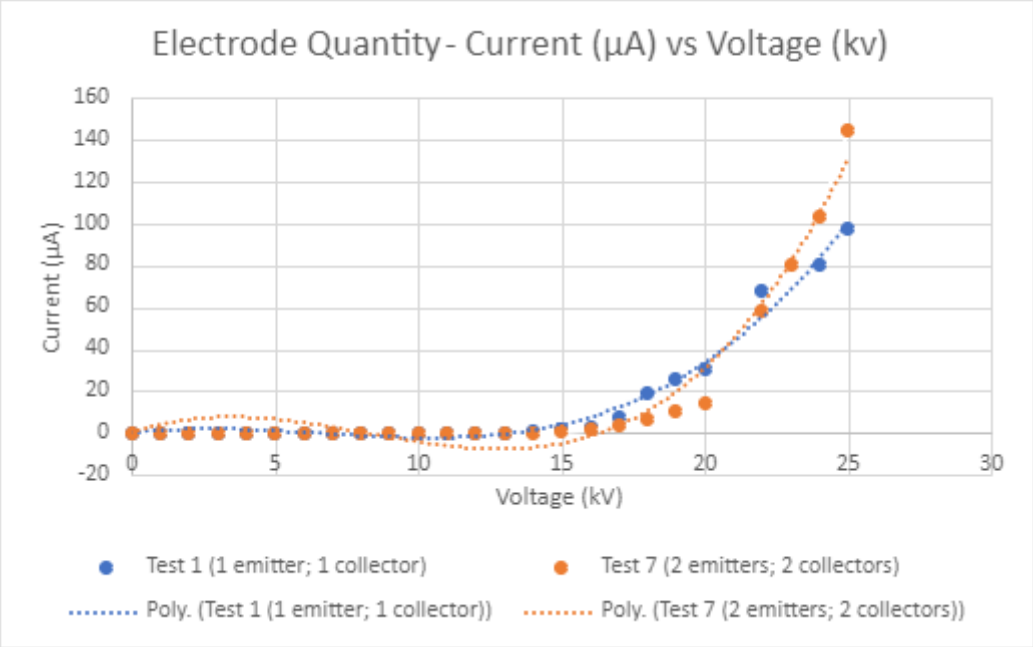

Figure 54: Current (µA) vs Voltage (kV) for Different Electrode Quantities

As shown in Figure 53, increasing the quantity of collector-emitter pairs increases thrust. Figure 54 shows that increasing the quantity of collector-emitter pairs slightly increases the current measured by the multimeter at higher voltages as well.

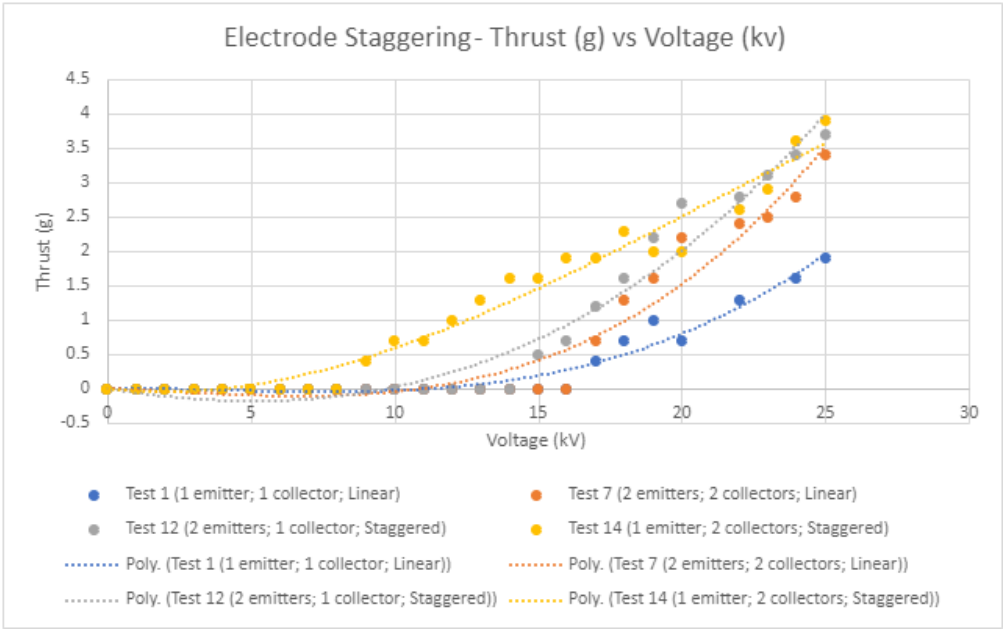

Figure 55: Thrust (g) vs Voltage (kV) for Electrode Staggering

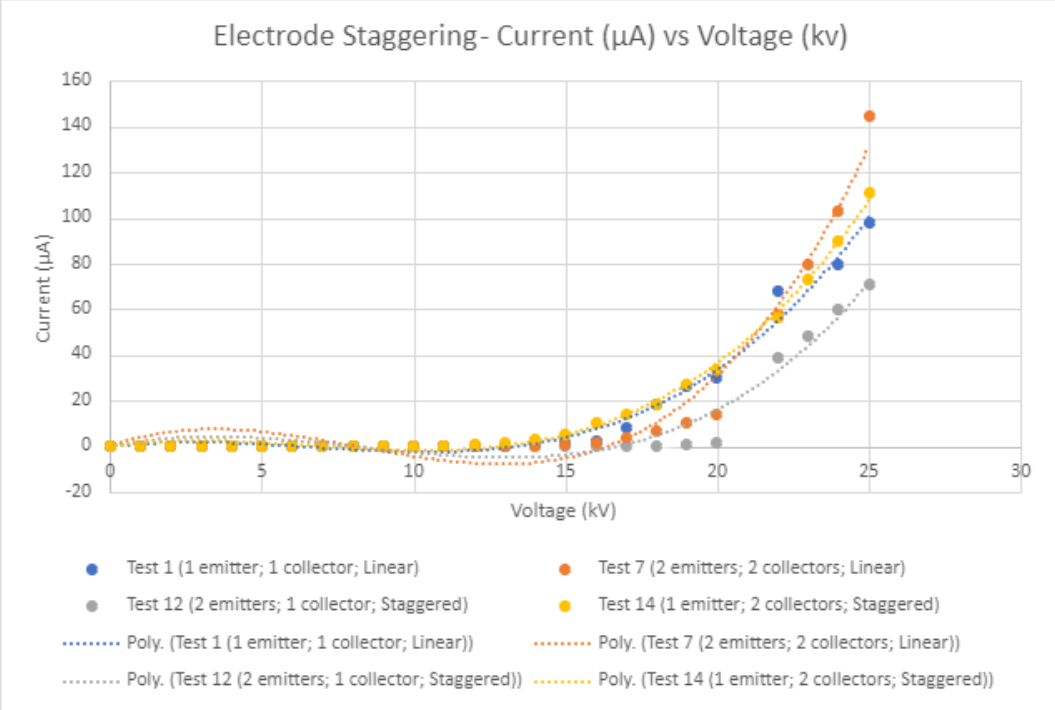

Figure 56: Current (µA) vs Voltage (kV) for Electrode Staggering

As shown in Figure 55, staggering the collectors and emitters increases thrust. Using 1 emitter and 2 collectors showed similar thrust performance to using 2 emitters and 1 collector. However, the former produces higher thrust values at the lower voltages. As expected, both of these configurations illustrated better performance than using 1 collector and 1 emitter in line with each other. A more surprising observation is that both configurations also exhibited better performance than a configuration with 2 emitters and 2 collectors in line. One would think that losing a collector or an emitter would reduce performance. However, it does the opposite. The team believes this is a result of a "nozzle effect" where instead of having an option to flow over or under the collector, ions and neutral air molecules are forced to flow between two collectors. This results in a more focused flow of ionic wind and in turn, an increase in the thrust produced. Figure 56 indicates that staggering the electrodes also slightly reduces the current measured by the multimeter, especially at higher voltages.

In summary, increasing collector diameter, decreasing the collector-emitter gap to a certain point while avoiding arcing, increasing the quantity of collector-emitter pairs, and staggering electrodes all

result in an increase in thrust density. These experiments achieved a thrust of up to 5.0 g or a thrust density of 321.74 $\frac{mN}{m}$ at 25 kV. In theory, the optimal electrode configuration with the available resources would be 4 or 5 electrode pairs (or as many that fit on the rig as possible) in a staggered configuration with $\frac{1}{2}$ inch collectors and a 1.5 inch collector-emitter gap. The spacing between collectors is another parameter that could be tested with more time.

4.7.3 Future Recommendations

For future project work, the team recommends updating the experiment rig. The 24" length of the rig is unnecessary. This could be shortened to 4 inches or less and serve the same purpose. The collector mounting holes should also be drilled all the way through all collectors for ease of mounting instead of attempting to thread a nut inside each collector. A hinging door could also be added for ease of access to the rigs between tests. Other parameters such as collector spacing, additional configurations, electrode material, and electrode shapes including airfoils could be tested. The power sub team should continue to work on a custom power supply that produces the required voltage output, is light enough to fly, and can operate for long enough to sustain flight. The team recommends designing a small ionic wind propulsion engine based on these experimental results and COMSOL simulations in addition to potentially designing, building, and flight testing an ionic wind aircraft.

5. Conclusions

For the main portion of the project, a team of four students were responsible for designing an ionic wind propulsion apparatus, a finite element simulation of the model, and a lightweight, high-voltage portable battery to attach to the autonomous aerial vehicle. This report represents the work done by the propulsion and power sub teams. Each sub team were able to fulfill their responsibilities to develop the project, while giving recommendations for next year's team.

According to the known mathematical formulas, the ionic wind simulation model was set up and the simulation results were obtained. The simulations were successful when comparing results with the papers from Huang and Chen. The results show the ionic wind's numerical values can change by modifying the electrode system, including the applied voltage, collector electrode radius, electrode gap, and number of collector electrodes. The ionic wind's maximum value is located on both sides of the collector electrode, rather than between the two electrodes where the particles are colliding. Since the collector electrode's surface is uniform, ions gather at both sides of the collector accelerating the airflow nearby. A tail effect is also seen where the ions circulate back into the collector from behind, causing a large loss in velocity.

From the experiment, it was concluded that increasing collector diameter, decreasing the collector-emitter gap to a certain point while avoiding arcing, increasing the quantity of collector-emitter pairs, and staggering electrodes all result in an increase in thrust density. Theoretically, the optimal electrode configuration with the available resources would be 4 or 5 electrode pairs in a staggered configuration with $\frac{1}{2}$ inch collectors and a 1.5 inch collector-emitter gap. The validity of this statement can be explored through more testing.

6. References

ATSDR jet fuels JP-4 and JP-7 tox profile. Agency for Toxic Substances and Disease Registry. (1995). https://www.atsdr.cdc.gov/ToxProfiles/tp76.pdf

Bowles, J. (2023). The Next Generation of Ionic Plasma Thrusters (BSI MARK 2). https://youtu.be/yftKjkZHirc

Chen, S., Zhu, Y., Tu, J., & Feng, W. (2019). *Numerical investigation of an electrohydrodynamic driven aeroplane: electrical properties, ionic wind and flight performance.* J. Phys. D: Appl. Phys. 52 365203 DOI: 10.1088/1361-6463/ab2b2a https://iopscience.iop.org/article/10.1088/1361-6463/ab2b2a/meta

Christian, A., & Cabell, R. (2017). *Initial Investigation into the Psychoacoustic Properties of Small Unmanned Aerial System Noise*. Nasa Technical Reports Server. https://ntrs.nasa.gov/api/citations/20170005870/downloads/20170005870.pdf

Civil Aviation Authority. (2023). Emerging Technologies: The effects of eVTOL aircraft noise on humans. https://publicapps.caa.co.uk/docs/33/Noise%20measurements%20from%20eVTOL%20aircraft%20(CAP%202506).pdf

Frąckiewicz, M. (2023, March 10). *Examining the environmental impact of drones*. TS2 SPACE. https://ts2.space/en/examining-the-environmental-impact-of-drones/#:~:text=Studies%20have%20shown%20that%20drones%20emitting%20noise%20louder%20than%2075,an%20increase%20in%20air%20pollution.

He, Yiou et al. "Design and implementation of a lightweight high-voltage power converter for electro-aerodynamic propulsion." 2017 IEEE 18th Workshop on Control and Modeling for Power Electronics (COMPEL), July 2017, Stanford, California, USA, Institute of Electrical and Electronics Engineers (IEEE), August 2017 © 2017 IEEE

IEA. (2023, July 11). *Aviation*. IEA. https://www.iea.org/energy-system/transport/aviation

Nature 563, 532–535 (2018). A) Computer-generated rendering of the EAD aeroplane, B) Photograph of actual EAD aeroplane, C) Architechture of the high-voltage power converter (HVPC). https://www.researchgate.net/publication/329102366/figure/fig3/AS:731590699274248@1551436223128/Aeroplane-design-a-Computer-generated-rendering-of-the-EAD-aeroplane-b-Photograph-of.png

Navi, R. (2000). *Parallel Resonance*. Hyper Physics. http://hyperphysics.phy-astr.gsu.edu/hbase/electric/parres.html#c1

P. Huang, Z. -y. Xie, P. Liu, D. -p. Leng, J. -p. Zheng and S. Wang, "Ionic Wind Simulation of Wire-Aluminum Foil Electrode Structure Lifter in 2-D Space," in *IEEE Transactions on Plasma Science*, vol. 50, no. 3, pp. 566-573, March 2022, doi: 10.1109/TPS.2021.3135057.

Passchier-Vermeer, W., & Passchier, W. F. (2000, March). *Noise Exposure and Public Health*. Environmental Health Perspectives. https://ehp.niehs.nih.gov/doi/10.1289/ehp.00108s1123

Plouraboue, Franck. (2018). “Flying with Ionic Wind,” *Nature 563, 476-477*. doi: https://doi.org/10.1038/d41586-018-07411-z

Ramadhan, AA, Kapur, N, Summers, JL et al. (2017) Numerical modelling of electrohydrodynamic airflow induced in a wire-to-grid channel. Journal of Electrostatics, 87. pp. 123-139. ISSN 0304-3886. https://doi.org/10.1016/j.elstat.2017.04.004

S. Estahbanati and U. Schichler, "Experiments on the Thrust Generation of Ionic Wind Propulsion Systems," 2022 IEEE International Conference on High Voltage Engineering and Applications (ICHVE), Chongqing, China, 2022, pp. 1-4, doi: 10.1109/ICHVE53725.2022.9961343

Tanner_tech, and Instructables. “ZVS High Voltage Power Supply.” *Instructables*, Autodesk, 19 Sept. 2017, www.instructables.com/ZVS-High-Voltage-Power-Supply/.

Vladislav Yu. Khomich, Igor E. Rebrov, In-atmosphere electrohydrodynamic propulsion aircraft with wireless supply onboard, Journal of Electrostatics, Volume 95, 2018, Pages 1-12, ISSN 0304-3886, https://doi.org/10.1016/j.elstat.2018.07.005

Wilson, J., Perkins, H.D., & Thompson, W.K. (2009). An Investigation of Ionic Wind Propulsion.

World Wildlife Fund. (n.d.). *Cutting aviation pollution*. WWF. https://www.worldwildlife.org/initiatives/cutting-aviation-pollution#:~:text=Overview,-%C2%A9%20Mislik%20%2F%20Shutterstock&text=Aviation%20is%20one%20of%20the,polluting%20nations%20on%20the%20planet.

Xu, H., He, Y., Strobel, K.L. et al. Flight of an aeroplane with solid-state propulsion. Nature 563, 532–535 (2018). https://doi.org/10.1038/s41586-018-0707-9

Z. Zhang, "Corona Discharge Ion Wind Propulsion System Model Based on COMSOL," *2022 International Conference on Manufacturing, Industrial Automation and Electronics (ICMIAE)*, Rimini, Italy, 2022, pp. 184-190, doi: 10.1109/ICMIAE57032.2022.00042.